Electronic Supporting Information (ESI) to accompany by:

Metal-Organic Frameworks with Potential for Energy-Efficient Adsorptive Separation of Light Hydrocarbons

Yabing He,[a] Rajamani Krishna,*[b] Banglin Chen*[a]

[a] Department of Chemistry, University of Texas at San Antonio

One UTSA Circle, San Antonio, Texas 78249-0698, USA

[b] Van 't Hoff Institute for Molecular Sciences, University of Amsterdam, Science Park 904,

1098 XH Amsterdam, The Netherlands

Table of Contents

1. MOF structures investigated for the light hydrocarbon separations

Table S1 summarizes the structural data on 19 different MOFs synthesized in this study for the purpose of evaluating their efficacies in separation of light hydrocarbon mixtures. The chosen MOFs cover a wide range of framework types, such as ones with open metal sites (e.g. **MgMOF-74**, **CoMOF-74**, **CuBTC**), mixed metallo-ligands (M'MOFs), etc. *Figure S1* presents the single-crystal structures of some typical MOFs such as **CuBTC**, **UTSA-20**, **MOF-505** (isostructural with **PCN-16**, **NOT-101** and **NOTT-102**), and **UMCM-150**. The organic linkers used to construct MOFs investigated are shown in *Scheme S1*.

Table S1. Structural data on the different MOFs evaluated in this study for $C_1/C_2/C_3$ separation.

MOFs	Langmuir surface area [$m^2\ g^{-1}$]	Pore volume [$cm^3\ g^{-1}$]	Framework density [$kg\ m^{-3}$]
CoMOF-74	1448.5[a]	0.5146	1169
MgMOF-74	1668.5[a]	0.6071	909
CuBTC (= HKUST-1)	2139.1[a]	0.7634	879
MOF-505	1703.7[a]	0.6086	926.5
PCN-16	2809.7[a]	0.9987	717.9
UMCM-150	3330.4[a]	1.2086	635.7
NOTT-101	2929.8[a]	1.0485	683.8
NOTT-102	3590.1[a]	1.2807	587.2
UTSA-20	1894.1[a]	0.6745	909.6
UTSA-33a	1024.1[a]	0.3673	993
UTSA-34a	937.0[a]	0.3336	889.8
UTSA-34b	1532.6[a]	0.5419	840.4
UTSA-35a	875.0[a]	0.3133	1046
M'MOF-2a	939[b]	0.301	997
M'MOF-3a	551[b]	0.165	1023
M'MOF-4a		0.289	1126
M'MOF-5a		0.126	1039
M'MOF-6a		0.216	1078
M'MOF-7a		0.045	1037

a) Calculated from N_2 adsorption isotherm at 77 K; b) Calculated from CO_2 adsorption isotherm at 196 K.

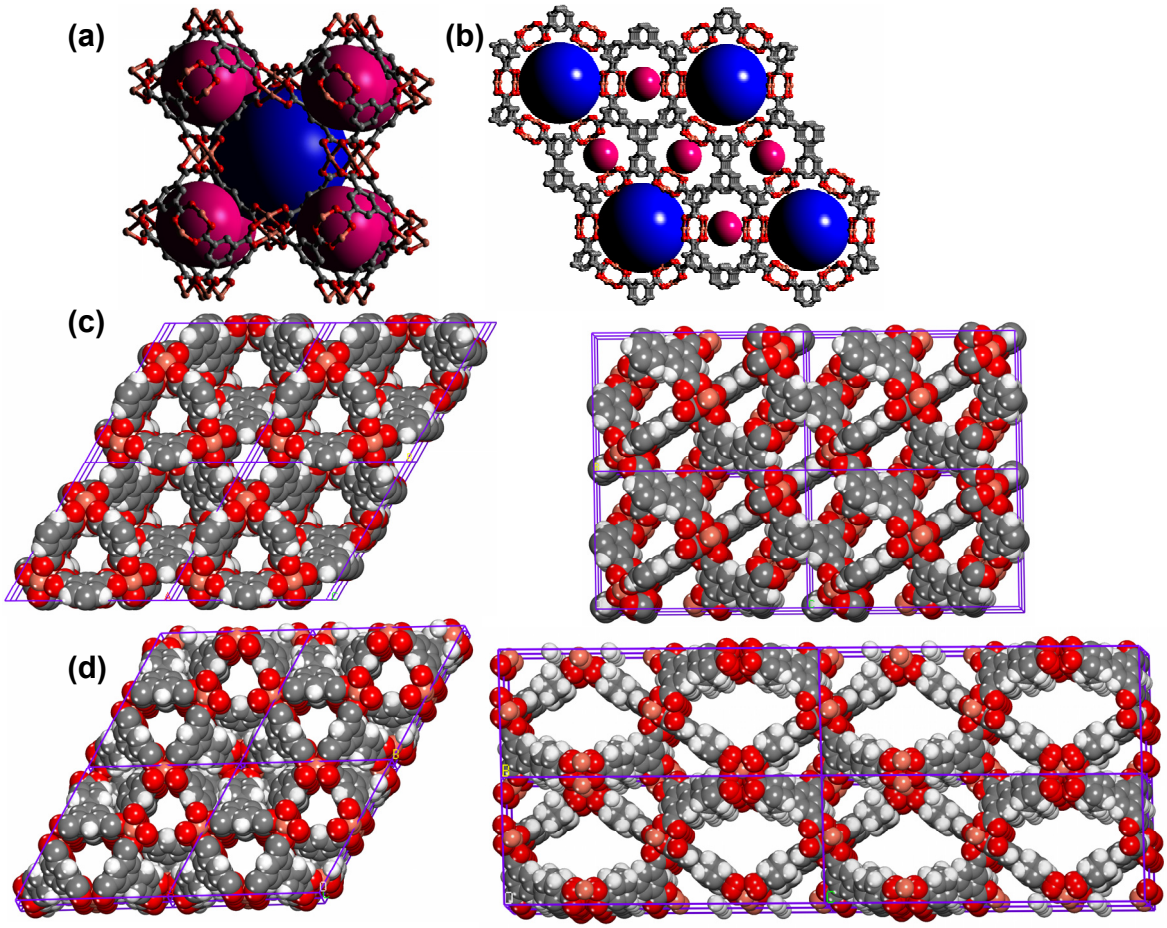

Figure S1. The X-ray single-crystal structures of **CuBTC** (a), **UTSA-20** (b), **MOF-505** (c), and **UMCM-150** (d).

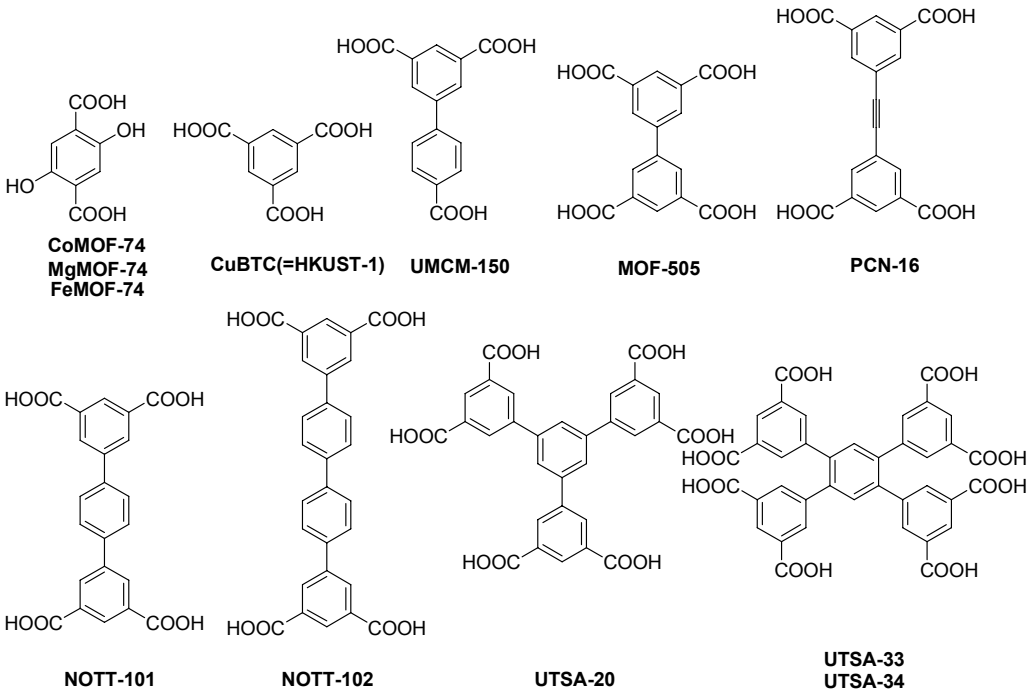

Scheme S1. The organic linkers used to construct the MOFs investigated.

2. Details of synthesis of MOFs

CoMOF-74,[1] **MgMOF-74**,[2, 3] **CuBTC** (= **HKUST-1**),[4] **MOF-505**,[5] **PCN-16**,[6, 7] **UMCM-150**,[8] **NOTT-101**,[9] **NOTT-102**,[9] **UTSA-20**,[10] **UTSA-33**,[11] **UTSA-34**,[12] **UTSA-35**,[13] **M'MOF-2**,[14] **M'MOF-3**,[14] **M'MOF-4**,[15] **M'MOF-5**,[15] **M'MOF-6**,[15] and **M'MOF-7**[15] were prepared according to the corresponding reported references. The experimental powder X-ray diffraction (PXRD) patterns are in good agreement with the simulated PXRD patterns (*Figure S2*). Their detailed synthetic procedures and activation profiles are given below.

CoMOF-74: 2,5-dihydroxyterephthalic acid (H_4dobdc, 19.3 mg, 97.4 μmol, Aldrich) and $Co(NO_3)_2 \cdot 6H_2O$ (95.1 mg, 326.8 μmol, Acros) were mixed and dispersed in DMF/EtOH/H_2O (*v*/*v*/*v*, 1:1:1, 8.0 mL) in a vial (20 mL). The suspension was sonicated until homogeneous. The vial was capped tightly and placed in an oven at 100 ^oC. After 24 h, the vial was removed from the oven and allowed to cool to room temperature. The microcrystals were collected and washed with DMF. The sample was solvent-exchanged with dry methanol at least 10 times, and vacuumed at room temperature for 24 h, and then at 200 ^oC for 24 h and finally at 250 ^oC for 8 h to generate the activated sample.

MgMOF-74: 2,5-dihydroxyterephthalic acid (H_4dobdc, 22.2 mg, 112.0 μmol, Aldrich) and $Mg(NO_3)_2 \cdot 6H_2O$ (95.0 mg, 370.5 μmol, Acros) were mixed and dispersed in DMF/EtOH/H_2O (*v*/*v*/*v*, 15/1/1, 10.0 mL) in a vial (20 mL). The suspension was sonicated until homogenous. The vial was capped tightly and placed in an oven at 125 ^oC. After 20 h, the vial was removed from the oven and allowed to cool to room temperature. The resulting yellow microcrystals were collected and washed with DMF. The sample was solvent-exchanged with dry methanol at least 10 times. The solvent was removed under high vacuum at room temperature for 24 h, and then at 200 ^oC for 24 h and finally at 250 ^oC for 8 h, yielding the activated sample.

CuBTC: A solution of $Cu(NO_3)_2 \cdot 2.5H_2O$ (124.0 mg, 533.1 μmol, Aldrich) and 1,3,5-benzenetricarboxylic acid (H_3btc, 74.0 mg, 352.1 μmol, Aldrich) in the mixed solvents of DMF/EtOH/H_2O (*v*/*v*/*v*, 1/1/1, 18.0 mL) in a capped vial (20 mL) was kept at 75 ^oC for 24 h to give green cubic microcrystalline crystals. The fresh sample was guest-exchanged with dry acetone, and outgassed under high vacuum at room temperature for 24 h, and then at 120 ^oC until the degassed rate is 5 μmHg min^{-1} to generate the activated sample.

MOF-505: Biphenyl-3,3',5,5'-tetracarboxylic acid (H_4bptc, 50.0 mg, 151.4 μmol) and $Cu(NO_3)_2 \cdot 2.5H_2O$ (100.0 mg, 429.9 μmol, Aldrich) were mixed and dispersed in DMF/1,4-dioxane/H_2O (*v*/*v*/*v*, 2/1/1, 15.0 mL). The resulting slurry mixture turned clear upon addition of 2 drops of aqueous HCl (37%). The solution was heated at 80 ^oC for 72 hrs. The fresh sample was solvent-exchanged with dry acetone, and vacuumed at room temperature for 24 h, and then at 120 ^oC until the degassed rate is 5 μmHg min^{-1} to yield the activated **MOF-505**.

PCN-16: A mixture of 5,5'-(1,2-ethynediyl)bis(1,3-benzenedicarboxylic acid) (H_4ebdc, 10.0 mg, 28.2 μmol), $Cu(NO_3)_2 \cdot 2.5H_2O$ (20.0 mg, 86.0 μmol, Aldrich) and 2 drops of HBF_4 (48-50%, fisher) in 1.5 mL of *N*,*N*'-dimethylacetamide (DMA) was placed in a vial (20 mL). The vial was capped tightly and placed in an oven at 75 ^oC for 72 h. The resulting crystals were collected and washed with DMA. The fresh sample was solvent-exchanged with dry methanol, and vacuumed at room temperature for 24 h, and then at 100 ^oC until the degassed rate is 5 μmHg min^{-1} to yield the activated **PCN-16**.

UMCM-150: Biphenyl-3,4',5-tricarboxylic acid (H_3bpt, 50.0 mg, 174.7 μmol) and $Cu(NO_3)_2 \cdot 2.5H_2O$ (98.0 mg, mol, 421.3 μmol, Aldrich) were dissolved in DMF/1,4-dioxane/H_2O (*v*/*v*/*v*, 4/1/1, 15 mL). The solution was placed in a tightly capped vial (20 mL) and heated at 85 ^oC for 6 h. The crystals were collected and washed with fresh DMF. The sample was solvent-exchanged with dry acetone, and outgassed at room temperature for 24 h, and then at 100 ^oC until the degassed rate is 5 μmHg min^{-1} to yield the activated **UMCM-150**.

NOTT-101: Terphenyl-3,3'',5,5''-tetracarboxylic acid (H_4tptc, 50.00 mg, 123.0 μmol) and $Cu(NO_3)_2 \cdot 2.5H_2O$ (100.0 mg, 429.9 μmol, Aldrich) were mixed and dispersed in DMF/1,4-dioxane/H_2O (*v*/*v*/*v*, 2/1/1, 15.0 mL). The resulting slurry turned clear upon addition of 2 drops of aqueous HCl (36%). The solution was heated to 80 ^oC and kept at this temperature for 3 days. The sample was solvent-exchanged with dry acetone, and vacuumed at room temperature for 24 h, and at 100 ^oC until the degassed rate is 5 μmHg min^{-1} to yield the activated **NOTT-101**.

NOTT-102: Quaterphenyl-3,3''',5,5'''-tetracarboxylic acid (H_4qptc, 50.0 mg, 103.6 μmol) and $Cu(NO_3)_2 \cdot 2.5H_2O$ (100.0 mg, 429.9 μmol, Aldrich) were mixed and dispersed in DMF/1,4-dioxane/H_2O (*v*/*v*/*v*, 2/1/1, 15.0 mL). The resulting slurry turned clear upon addition of 2 drops of aqueous HCl (36%). The solution was heated to 80 ^oC and kept at this temperature for 3 days. The sample was solvent-exchanged with dry acetone, and vacuumed at room temperature for 24 h, and then at 100 ^oC until the degassed rate is 5 μmHg min^{-1} to yield the activated **NOTT-102**.

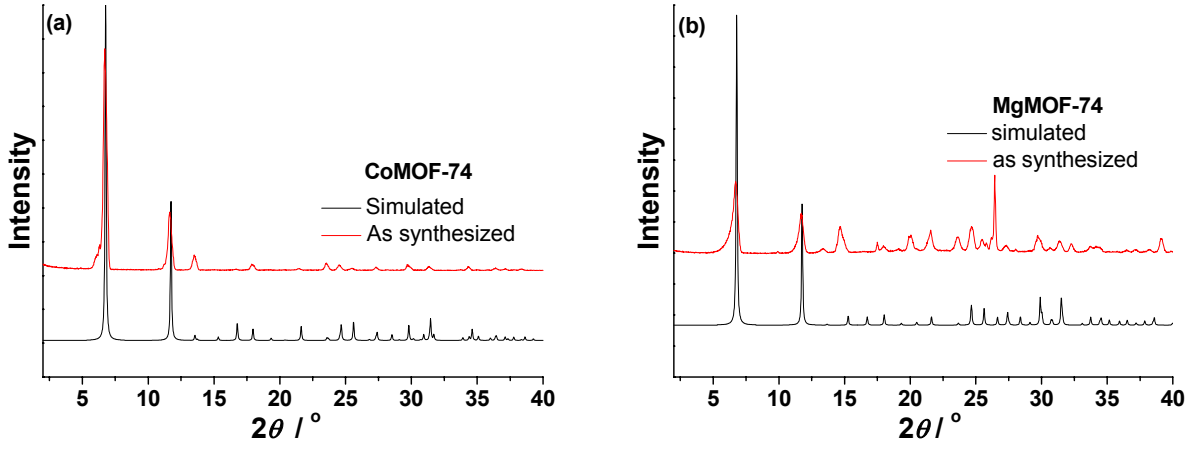

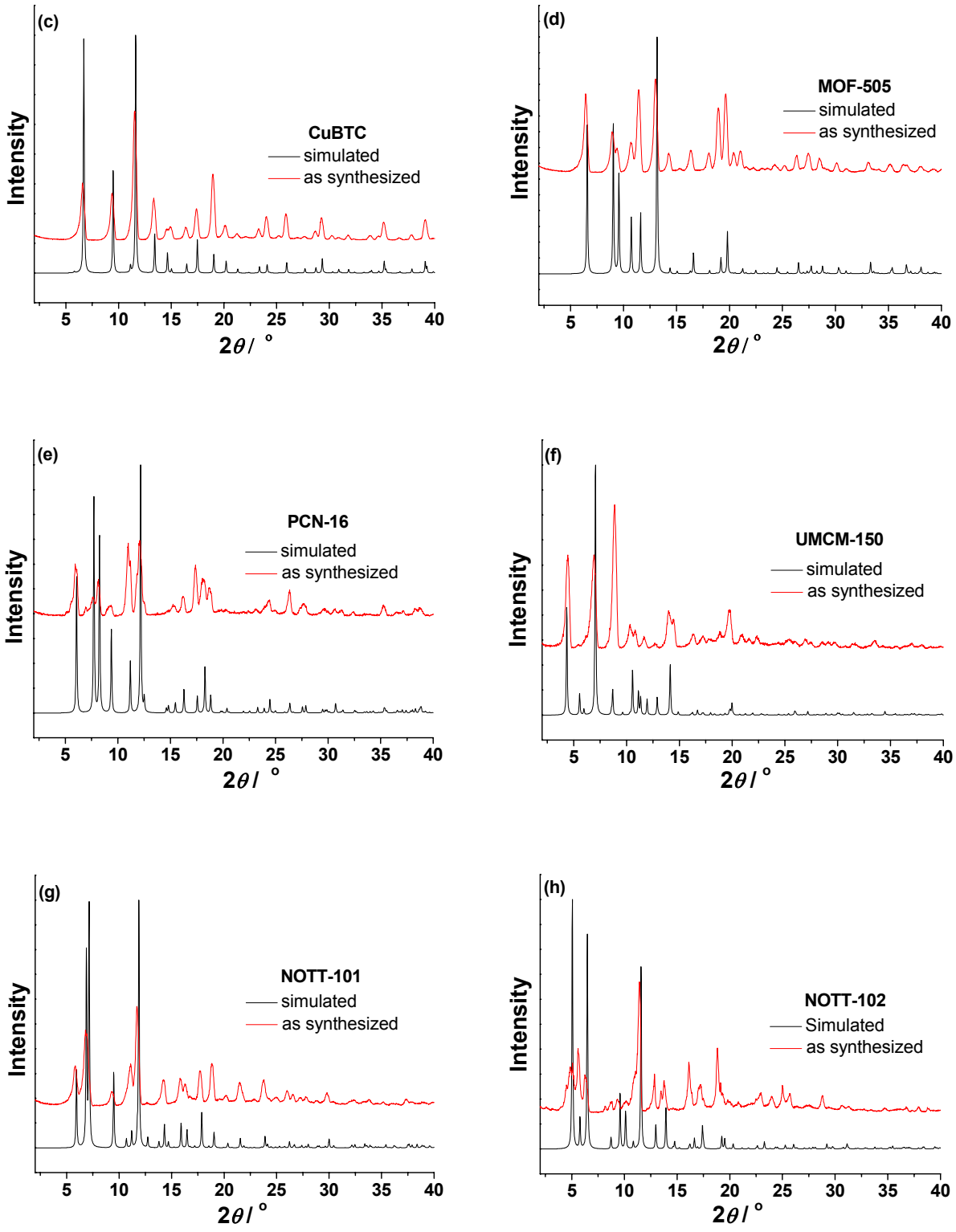

Figure S2. PXRD patterns of **CoMOF-74** (a), **MgMOF-74** (b), **CuBTC** (c), **MOF-505** (d), **PCN-16** (e), **UMCM-150** (f), **NOTT-101** (g), and **NOTT-102** (h).

3. Measurement of pure-component isotherms of light hydrocarbons in different MOFs

A Micromeritics ASAP 2020 surface area analyzer was used to measure gas sorption isotherms. C_2H_2 (atomic absorption grade) was purchased from western international gas & cylinders Inc.; C_2H_4 (2.5 N), C_2H_6 (2.0 N) were purchased from conley gas ltd.; CH_4 (3.7 N), C_3H_6, and C_3H_8 were purchased from Praxair Inc. and used as received. 100-150 mg of the samples were used in gas sorption measurements and maintained at 77 K with liquid nitrogen, at 273 K with an ice–water bath. As the center–controlled air conditioner was set up at 23 ^oC, a water bath was used for adsorption isotherms at 296 K.

Before measurement of sorption isotherms of light hydrocarbons, their N_2 isotherms at 77 K were also examined (*Figure S3*), and are in good agreement with the reported data except for **NOTT-101** and **NOTT-102**. Our measured surface areas for **NOTT-101** and **NOTT-102** are higher than those reported by Lin et al,[9] and are in good agreement with the values obtained from the single-crystal data. The surface areas and pore volumes determined from N_2 isotherms at 77 K were summarized in *Table S1*. *Figures S4-22* present CH_4, C_2H_2, C_2H_4, and C_2H_6 sorption isotherms for all MOFs investigated in the paper. C_3H_6 and C_3H_8 isotherms for **CoMOF-74** are also included in *Figure S4*.

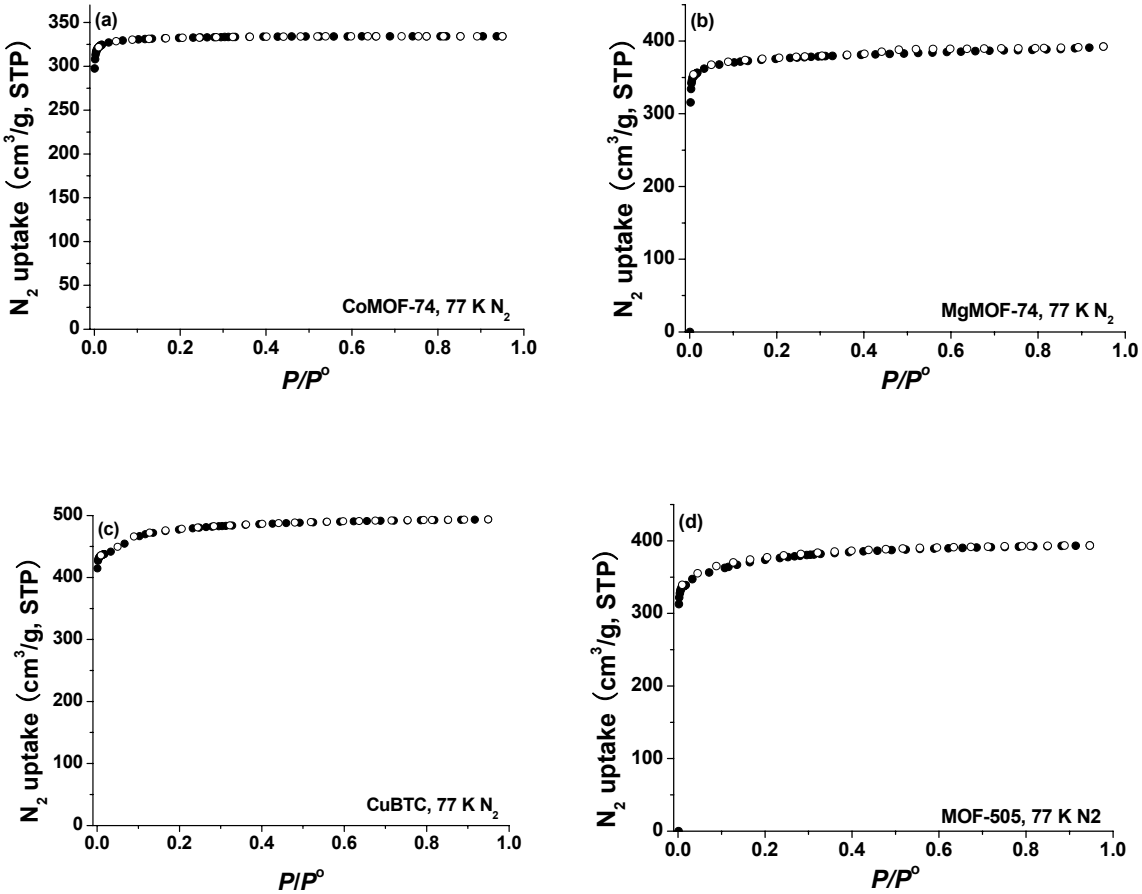

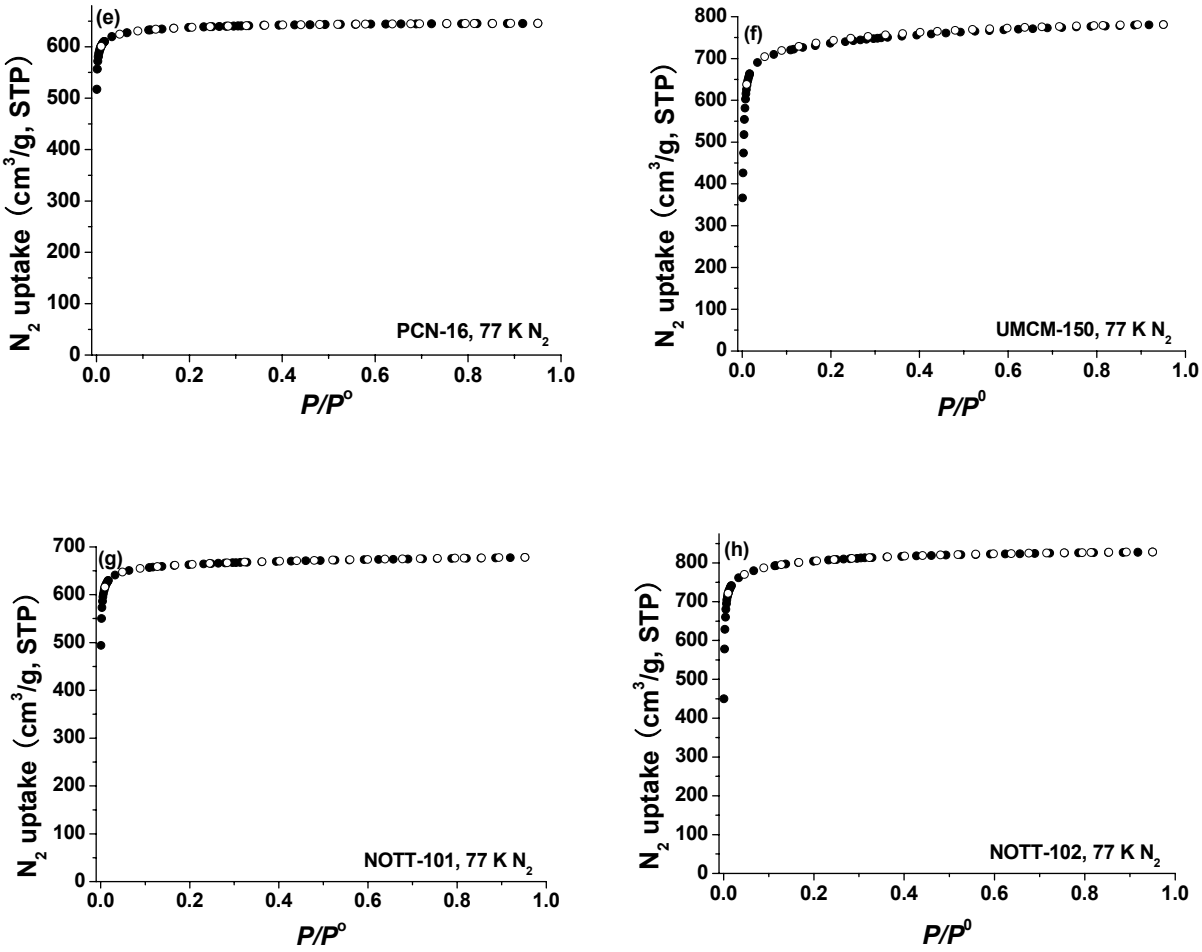

Figure S3. N_2 sorption isotherms of **CoMOF-74** (a), **MgMOF-74** (b), **CuBTC** (c), **MOF-505** (d), **PCN-16** (e), **UMCM-150** (f), **NOTT-101** (g), and **NOTT-102** (h) at 77 K. Solid symbols: adsorption, open symbols: desorption.

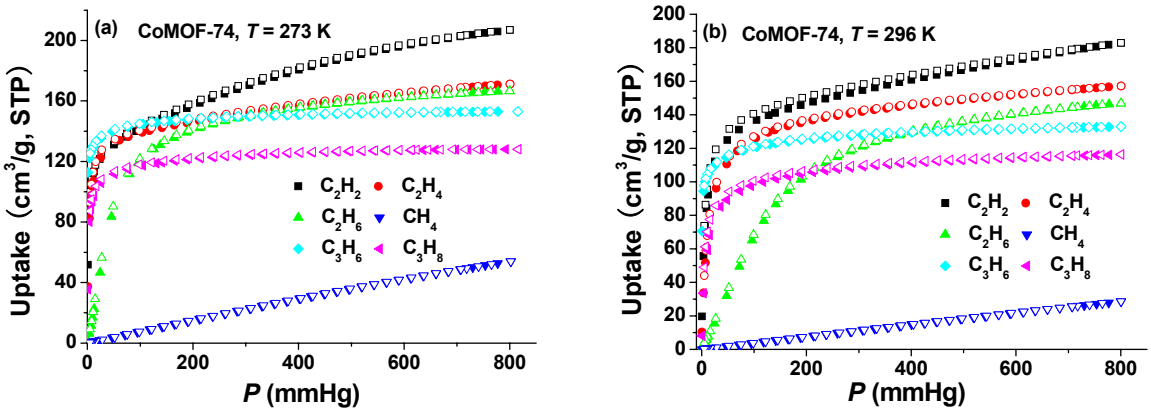

Figure S4. C_2H_2, C_2H_4, C_2H_6, and CH_4 sorption isotherms of **CoMOF-74** at 273 K (a), and 296 K (b). Solid symbols: adsorption, open symbols: desorption.

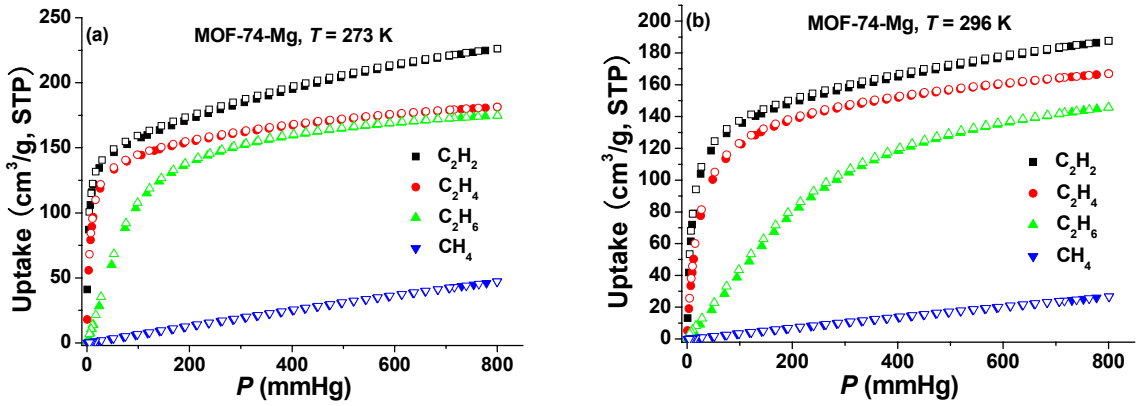

Figure S5. C_2H_2, C_2H_4, C_2H_6, and CH_4 sorption isotherms of **MgMOF-74** at 273 K (a), and 296 K (b). Solid symbols: adsorption, open symbols: desorption.

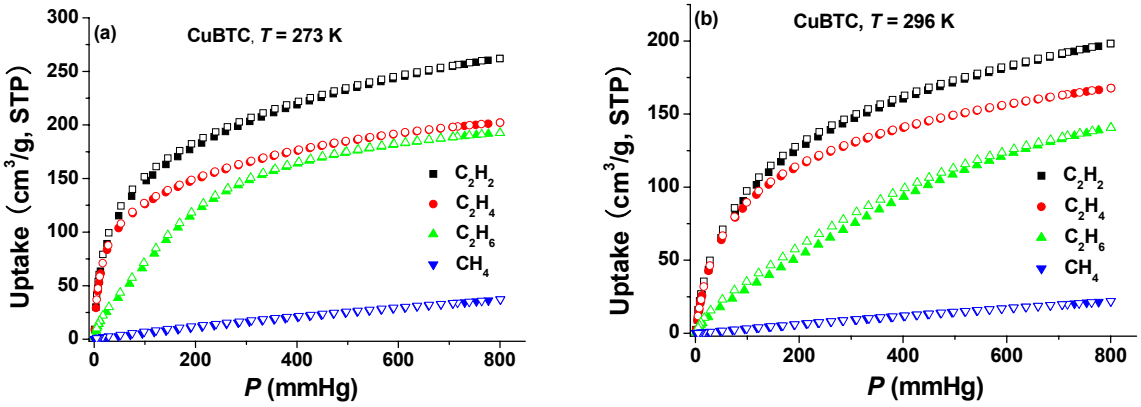

Figure S6. C_2H_2, C_2H_4, C_2H_6, and CH_4 sorption isotherms of **CuBTC** at 273 K (a), and 296 K (b). Solid symbols: adsorption, open symbols: desorption.

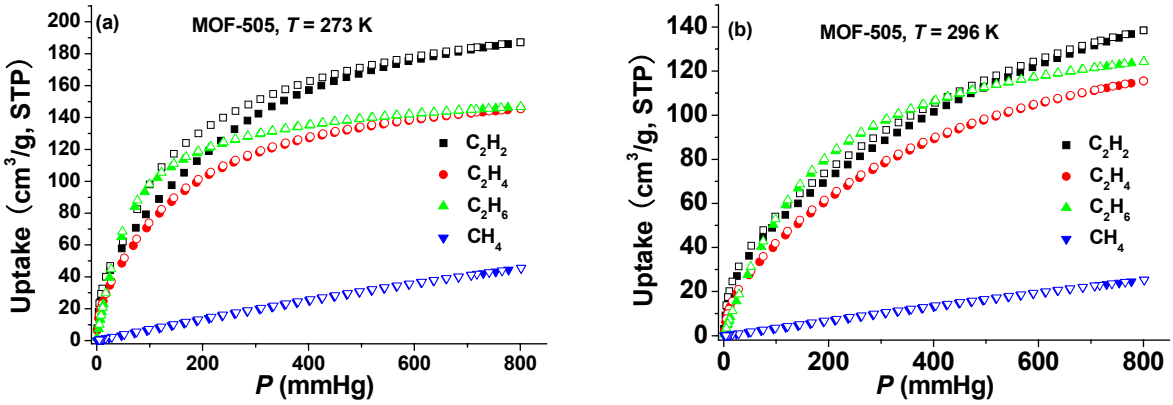

Figure S7. C_2H_2, C_2H_4, C_2H_6, and CH_4 sorption isotherms of **MOF-505** at 273 K (a), and 296 K (b). Solid symbols: adsorption, open symbols: desorption.

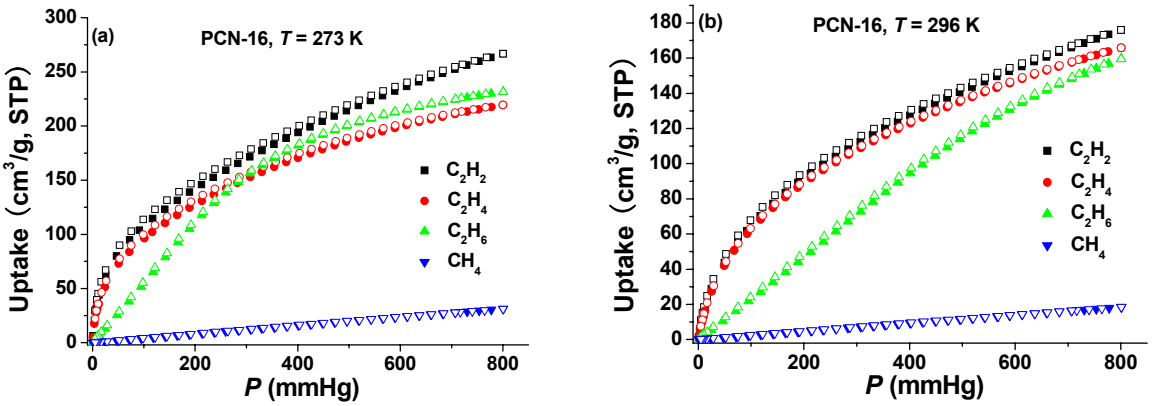

Figure S8. C_2H_2, C_2H_4, C_2H_6, and CH_4 sorption isotherms of **PCN-16** at 273 K (a), and 296 K (b). Solid symbols: adsorption, open symbols: desorption.

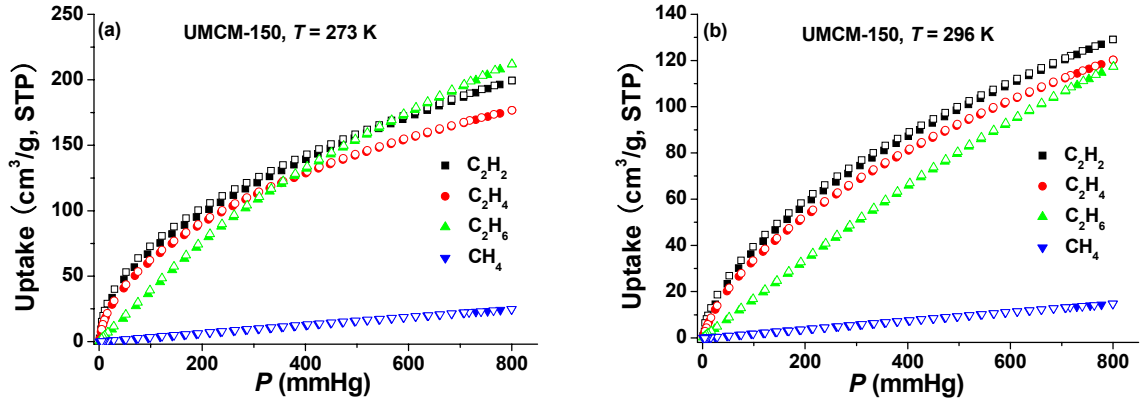

Figure S9. C_2H_2, C_2H_4, C_2H_6, and CH_4 sorption isotherms of **UMCM-150** at 273 K (a), and 296 K (b). Solid symbols: adsorption, open symbols: desorption.

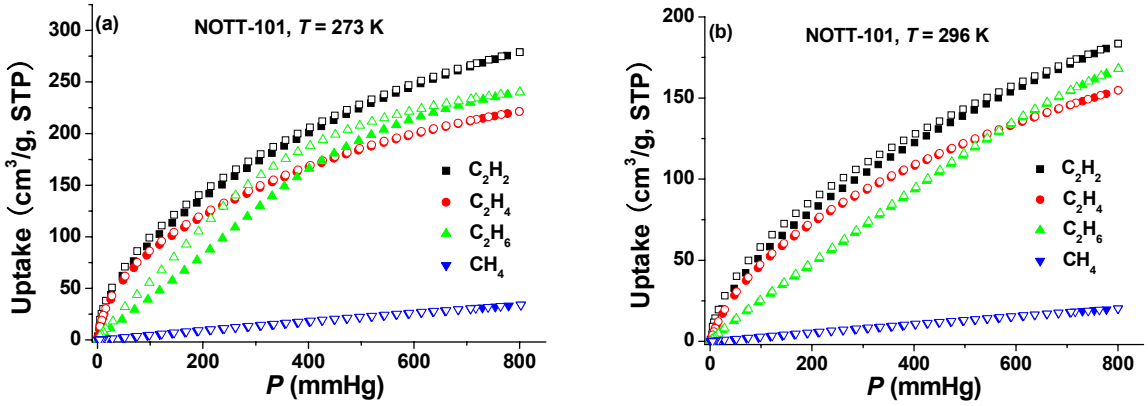

Figure S10. C_2H_2, C_2H_4, C_2H_6, and CH_4 sorption isotherms of **NOTT-101** at 273 K (a), and 296 K (b). Solid symbols: adsorption, open symbols: desorption.

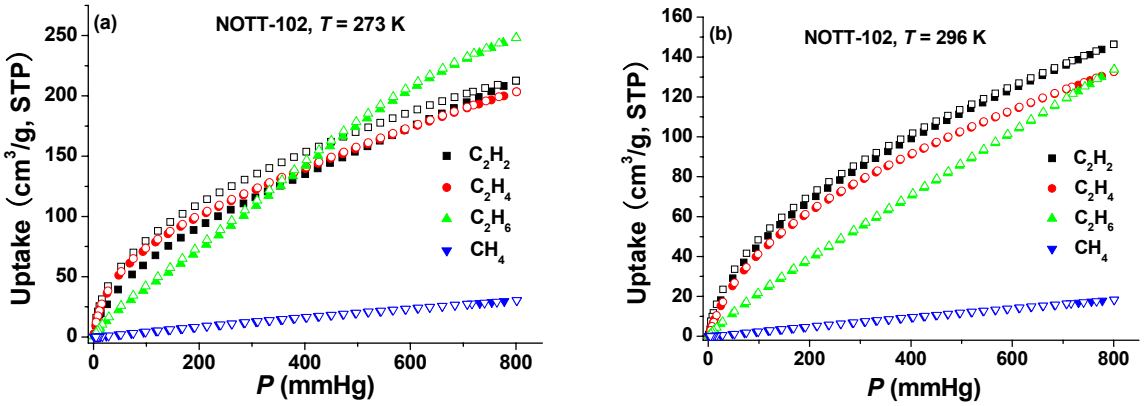

Figure S11. C_2H_2, C_2H_4, C_2H_6, and CH_4 sorption isotherms of **NOTT-102** at 273 K (a), and 296 K (b). Solid symbols: adsorption, open symbols: desorption.

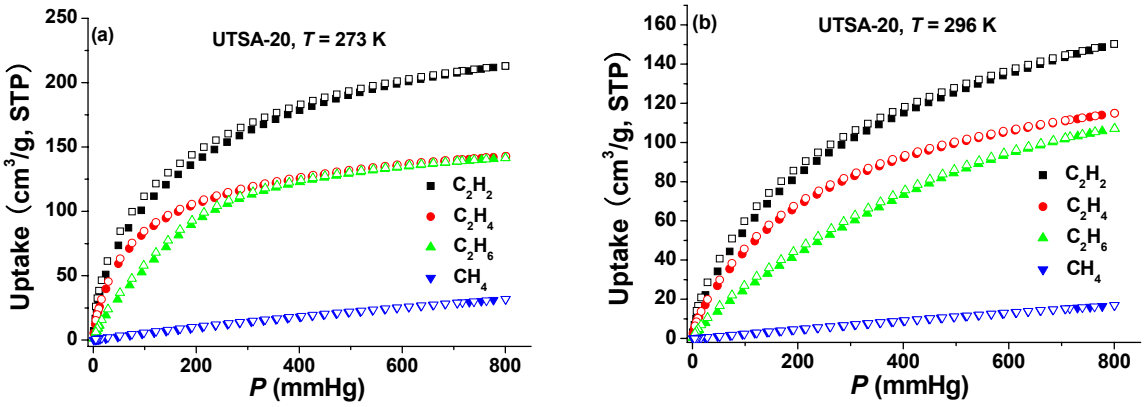

Figure S12. C_2H_2, C_2H_4, C_2H_6, and CH_4 sorption isotherms of **UTSA-20** at 273 K (a), and 296 K (b). Solid symbols: adsorption, open symbols: desorption.

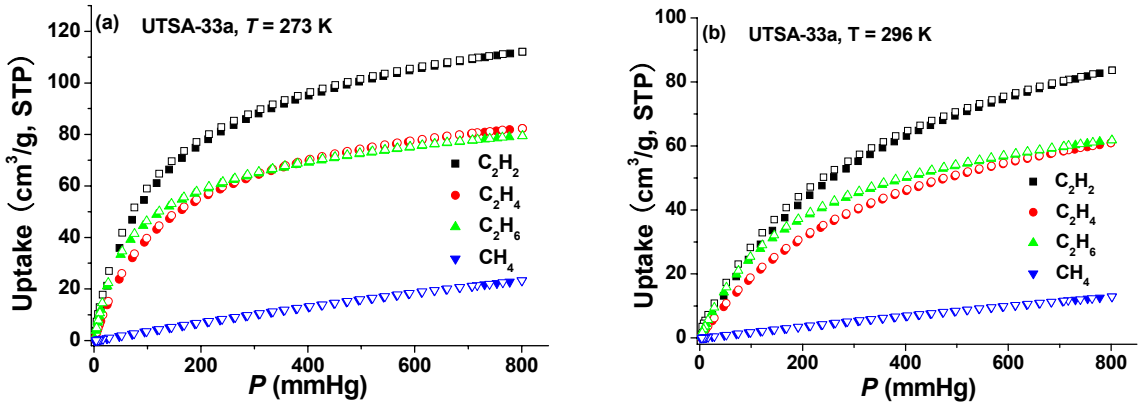

Figure S13. C_2H_2, C_2H_4, C_2H_6, and CH_4 sorption isotherms of **UTSA-33a** at 273 K (a), and 296 K (b). Solid symbols: adsorption, open symbols: desorption.

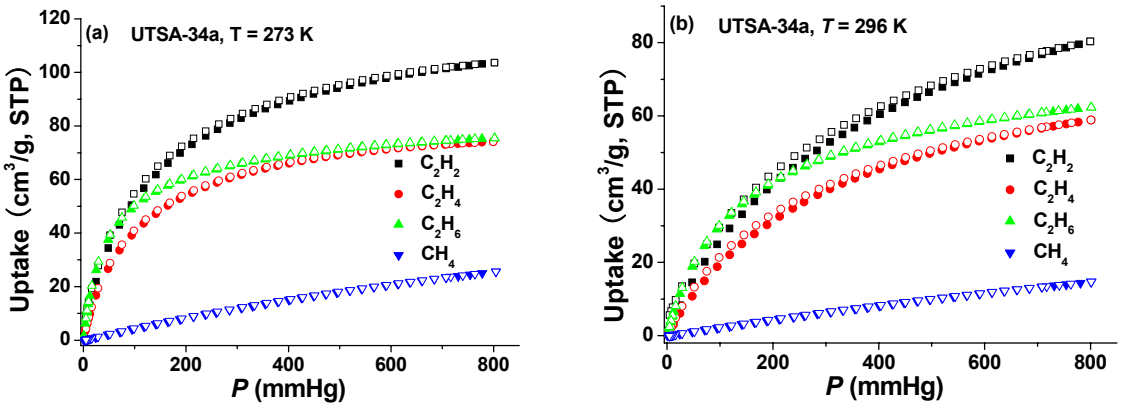

Figure S14. C_2H_2, C_2H_4, C_2H_6, and CH_4 sorption isotherms of **UTSA-34a** at 273 K (a), and 296 K (b). Solid symbols: adsorption, open symbols: desorption.

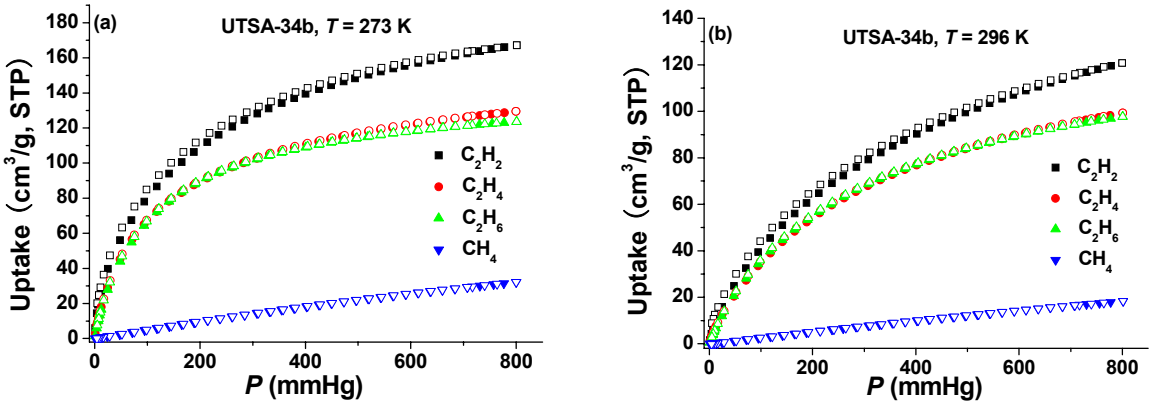

Figure S15. C_2H_2, C_2H_4, C_2H_6, and CH_4 isotherms of **UTSA-34b** at 273 K (a), and 296 K (b). Solid symbols: adsorption, open symbols: desorption.

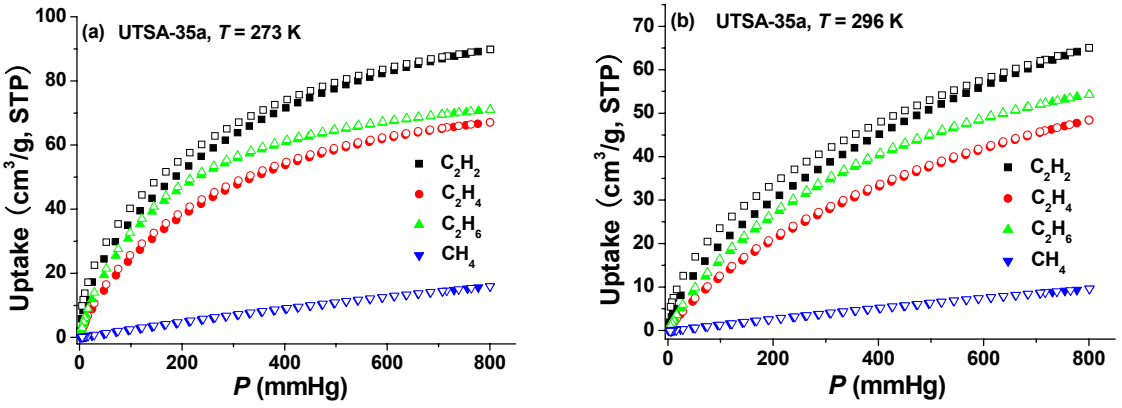

Figure S16. C_2H_2, C_2H_4, C_2H_6, and CH_4 sorption isotherms of **UTSA-35a** at 273 K (a), and 296 K (b). Solid symbols: adsorption, open symbols: desorption.

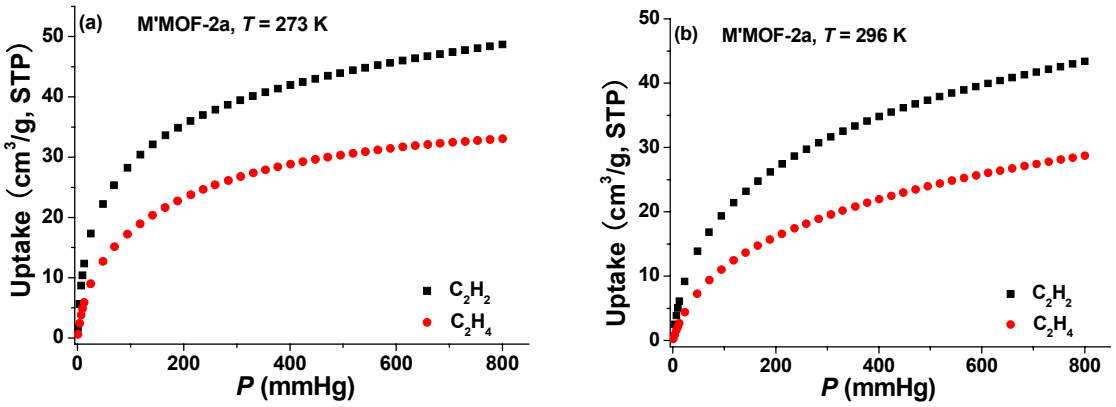

Figure S17. C_2H_2 and C_2H_4 adsorption isotherms of **M'MOF-2a** at 273 K (a), and 296 K (b).

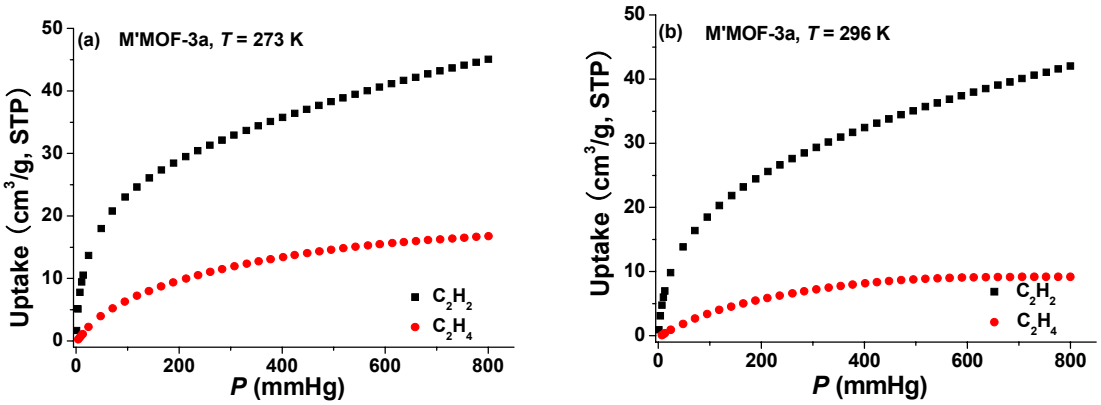

Figure S18. C_2H_2 and C_2H_4 adsorption isotherms of **M'MOF-3a** at 273 K (a), and 296 K (b).

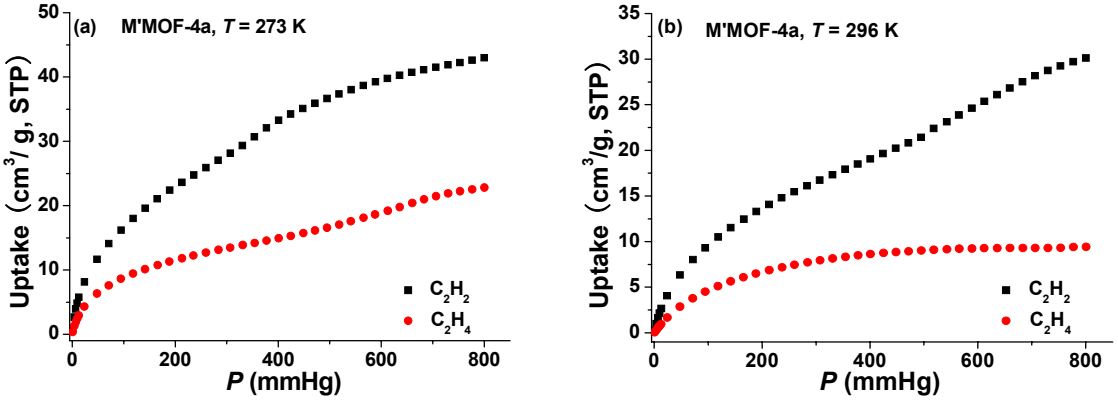

Figure S19. C_2H_2 and C_2H_4 adsorption isotherms of **M'MOF-4a** at 273 K (a), and 296 K (b).

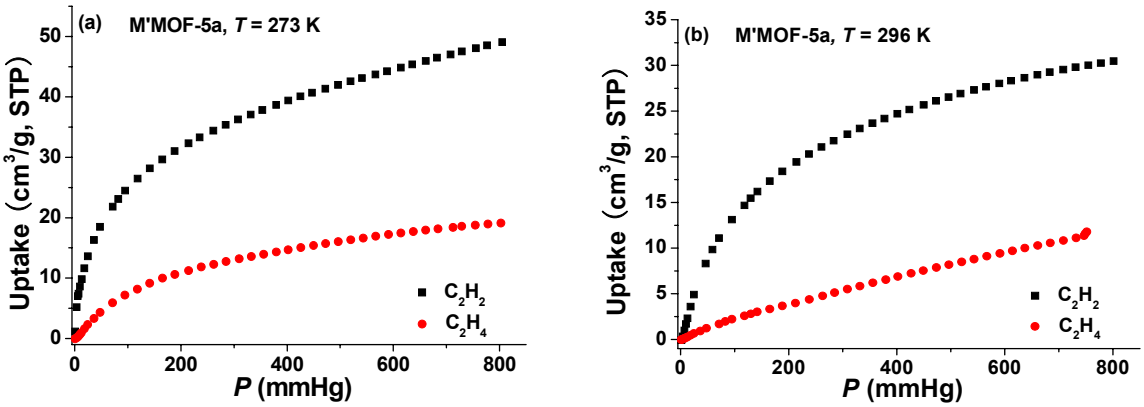

Figure S20. C_2H_2 and C_2H_4 adsorption isotherms of **M'MOF-5a** at 273 K (a), and 296 K (b).

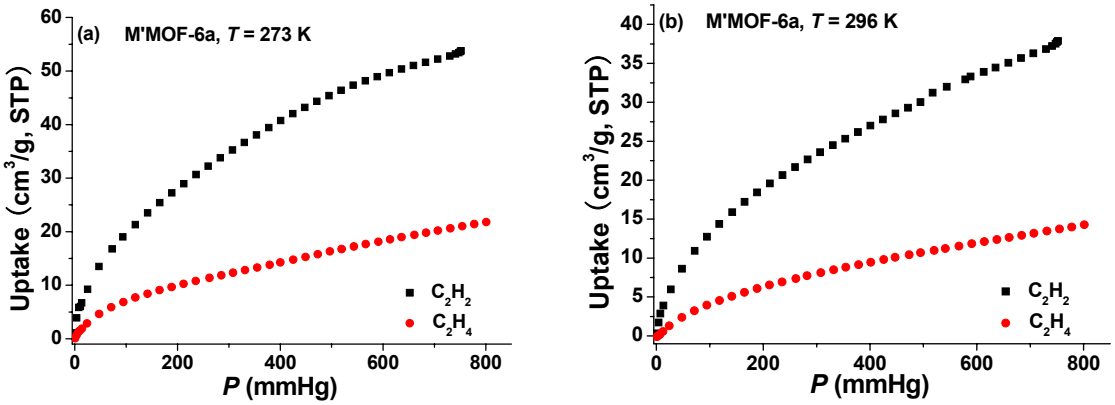

Figure S21. C_2H_2 and C_2H_4 adsorption isotherms of **M'MOF-6a** at 273 K (a), and 296 K (b).

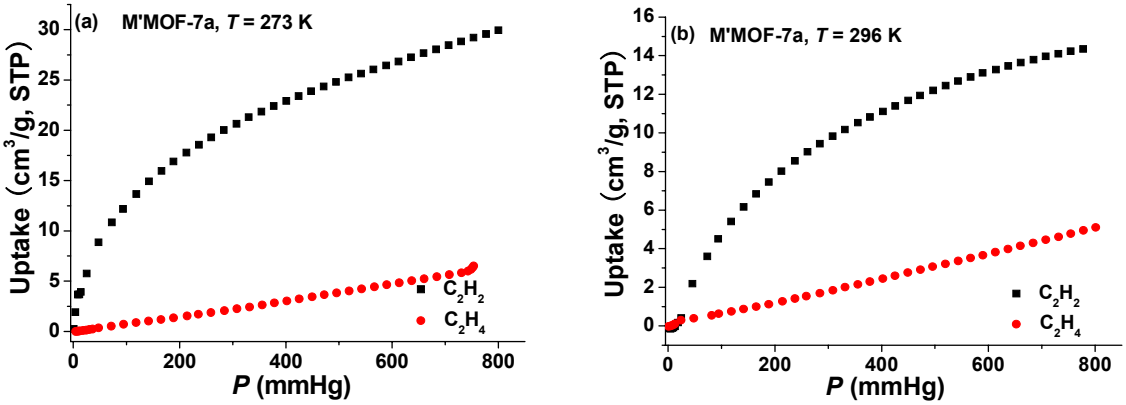

Figure S22. C_2H_2 and C_2H_4 adsorption isotherms of **M'MOF-7a** at 273 K (a), and 296 K (b).

4. Fitting of pure component isotherms

The measured experimental data on pure component isotherms for the 19 different MOFs, listed in *Table S1*, were first converted to absolute loading using the Peng-Robinson equation of state for estimation of the fluid densities. The pore volumes used for this purpose are those specified in *Table S1*.

The pure component isotherm data for CH_4, C_2H_2, C_2H_4, C_2H_6, C_3H_6, and C_3H_8, expressed in terms of *absolute* loadings, were fitted with the dual-site Langmuir-Freundlich isotherm model

$$q = q_{A,sat}\frac{b_A p^{\nu_A}}{1+b_A p^{\nu_A}} + q_{B,sat}\frac{b_B p^{\nu_B}}{1+b_B p^{\nu_B}} \quad (1)$$

with T-dependent parameters b_A, and b_B

$$b_A = b_{A0}\exp\left(\frac{E_A}{RT}\right); \quad b_B = b_{B0}\exp\left(\frac{E_B}{RT}\right) \quad (2)$$

The fitted parameter values for the 19 different MOFs, listed in *Table S1*, are presented in *Tables S3-S21*.

5. Pure component isotherm data from literature sources used in our evaluations of different MOFs

For evaluation of the light hydrocarbon separations with materials other than those synthesized and measured in our own investigations (as listed in *Table S1*), we have evaluated the performance of other MOFs, zeolites etc. using a variety of literature sources. *Table S2* provides the structural data for these additional adsorbents that have been evaluated in our study.

Table S2. Structural data on other materials evaluated in this study for light hydrocarbons separation for comparison purposes.

Adsorbents	Surface area [$m^2\ g^{-1}$]	Pore volume [$cm^3\ g^{-1}$]	Framework density [$kg\ m^{-3}$]
NaETS-10			1968
NaX zeolite	950	0.280	1421
FeMOF-74		0.626	1126
NiMOF-74		0.582	1194
FeMIL-100	2300	1.2	593
ZIF-8	1781	0.515	924

FeMOF-74

For evaluation of the light hydrocarbon separations with **FeMOF-74** (= **CPO-27-Fe** = Fe_2(dobdc)), the experimental pure-component isotherm data for ethyne, ethylene, ethane, methane, propylene, and propane at 318 K, 333 K, and 353 K. are reported by Bloch et al.[16] The measured isotherms reported in their experiments were refitted with *T*-dependent dual-site Langmuir-Freundlich parameters; these are provided in *Table S22*. For **FeMOF-74**, the separation performance is evaluated at 318 K, the lowest temperature used in their experiments.

MgMOF-74 isotherm data of Bao et al. [17, 18] and **Dietzel et al.**[19]

Bao et al.[18] report experimental isotherm data for CH_4 at 278 K, 298 K, and 318 K in **MgMOF-74** (= **CPO-27-Mg** = Mg_2(dobdc)). Dietzel et al.[19] report isotherm measurements for CH_4 at 283 K, 298K, 313 K, and 343 K in **MgMOF-74**. Our own experimental isotherm data for CH_4, measured at 273 K, and 296 K are in excellent agreement with these two data sets; this agreement is demonstrated by the observation that fitting individual data sets yields practically the same set of parameter values as by fitting the combined data sets from the three investigations. The dual-site Langmuir parameters for CH_4, obtained by fitting all three data sets are reported in *Table S20*.

Bao et al.[17] report the results of experimental isotherms for C_2H_4, C_2H_6, C_3H_6 and C_3H_8 in **MgMOF-74** at 278 K, 298 K, and 318 K. Our experimental isotherm data for C_2H_4, and C_2H_6 are in excellent agreement with their data set; this agreement is demonstrated by the observation that fitting individual data sets yields practically the same set of parameter values as by fitting the combined data sets from the two investigations. The dual-site Langmuir-Freundlich fit parameters for C_2H_4, C_2H_6, C_3H_6 and C_3H_8, obtained by fitting both sets of data are reported in *Table S20*.

CoMOF-74 isotherm data of Matzger et al. [20]

Our experimental isotherm data for C_2H_4 and C_2H_6 at 296 K in **CoMOF-74** (= **CPO-27-Co** = Co_2(dobdc)) are in good agreement with those presented in the US patent of Matzger et al.[20] (measured at 298 K); the fitted parameters reported in *Table S21* are obtained by fitting both data sets.

The Matzger patent[20] also presents pulse breakthrough experimental curves for C_2H_4/C_2H_6 and C_3H_6/C_3H_8 mixtures using **CoMOF-74**. Our breakthrough simulations for pulse inputs are compared with their breakthrough curves for experimental validation; here the parameters used are those reported in *Table S21*.

CuBTC for separation of mixtures containing propylene, and propane

For evaluation of the separation of C_3H_6/C_3H_8 mixtures we use the experimental isotherm data in the paper of Yoon et al.[21], measured at temperatures of 303 K, 313 K, 323 K, 333 K, and 353 K. These experimental data were re-fitted with the set of parameters specified in *Table S23.*

Yoon et al.[21] also report the results of breakthrough experiments that are used to validate our breakthrough simulation methodology; see below.

FeMIL-100

For comparison of the propylene/propane separation characteristics of **FeMIL-100**, experimental isotherm data at 303 K available in the paper by Yoon et al.[22] were fitted with a single-site Langmuir-Freundlich isotherm model. It is noteworthy that the pure component experimental data are available up to pressures of 7 kPa. Extrapolation to 100 kPa is therefore not justified. The calculations presented here are only up to a total pressure of 20 kPa. The single-site Langmuir-Freundlich fit parameters for propylene and propane isotherms in **FeMIL-100** at 303 K are given in *Table S24*.

NaX zeolite

For evaluation of the ethylene/ethane separation characteristics of **NaX** zeolite, the experimental data of Hyun and Danner[23], determined at temperatures T = 298 K, and 323 K were fitted with a dual-site Langmuir-Freundlich isotherm model. The parameters are provided in *Table S25*.

For propylene and propane adsorption in **NaX** zeolite, the data provided in Table 4 of the paper by Lamia et al.[24] were used; the parameter fits for T = 298 K, and 318 K are specified in *Table S26*.

NaETS-10

For evaluation of the ethylene/ethane separation characteristics of **NaETS-10** zeolite, the experimental isotherm data reported by Anson et al.[25] were used. The parameter values are provided in *Table S27*.

ZIF-8

ZIF-8 has been suggested for ethylene/ethane and propylene/propane separations,[26-28] but the performance of this material is based on diffusion effects, and not on the basis of adsorption strengths. We examine the separation performance of **ZIF-8** based on the data available in the literature sources.[26-28]

6. Packed bed adsorber breakthrough calculation methodology

It is now well recognized that the separation characteristics of a Pressure Swing Adsorption (PSA) unit is dictated by a *combination* of adsorption selectivity and uptake capacity.[29-31] For a rational choice of adsorbents for mixture separation, we need to have a proper method of evaluation that combines the selectivity and capacity metrics in a manner that is a true reflection of the separation performance of a PSA unit. For this purpose, we perform transient breakthrough calculations following the methodologies developed and described in earlier works.[29, 32-34]

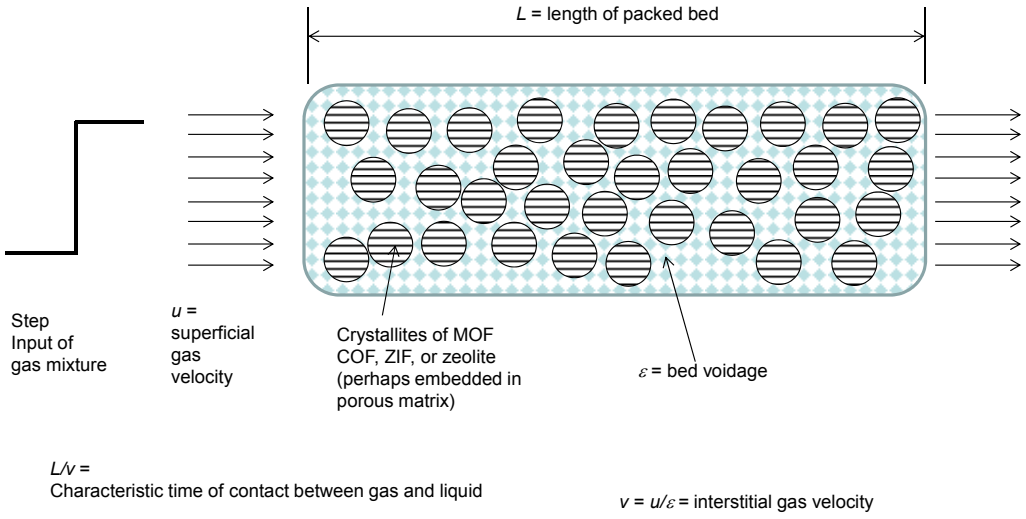

Figure S23. A schematic diagram of a packed bed adsorber.

Figure S23 shows a schematic of a packed bed adsorber bed of length L, packed with MOF, ZIF, COF, or zeolite crystals. Assuming plug flow of a n-component gas mixture through a fixed bed maintained under isothermal conditions, the partial pressures in the gas phase at any position and instant of time are obtained by solving the following set of partial differential equations for each of the species i in the gas mixture.[33, 35-40]

$$\frac{1}{RT}\frac{\partial p_i(t,z)}{\partial t} = -\frac{1}{RT}\frac{\partial\left(v(t,z)p_i(t,z)\right)}{\partial z} - \frac{(1-\varepsilon)}{\varepsilon}\rho\frac{\partial \bar{q}_t(t,z)}{\partial t}; \quad i = 1,2,...n \tag{3}$$

In equation (3), t is the time, z is the distance along the adsorber, ρ is the framework density, ε is the bed voidage, v is the interstitial gas velocity, and $\bar{q}_i$ is the *spatially averaged* molar loading within the crystallites of radius r_c:

$$\bar{q}_i(t,z) = \frac{3}{r_c^3}\int_0^{r_c} q_i(t,z)r^2 dr \tag{4}$$

Summing equation (4) over all n species in the mixture allows calculation of the *total average* molar loading of the mixture within the crystallite

$$\bar{q}_t(t,z) = \sum_{i=1}^{n}\bar{q}_i(t,z) \tag{5}$$

The *interstitial* gas velocity is related to the *superficial* gas velocity by

$$v = \frac{u}{\varepsilon} \tag{6}$$

Summing equation (3) over the n species present in the mixture, we obtain

$$\frac{1}{RT}p_t\frac{\partial(v(t,z))}{\partial z}=-\frac{(1-\varepsilon)}{\varepsilon}\rho\frac{\partial\bar{q}_t(t,z)}{\partial t} \tag{7}$$

where we have involved the assumption of negligible pressure drop, i.e.

$$\frac{\partial p_t}{\partial t}=0 \tag{8}$$

The molar loadings at the *outer surface* of the crystallites, i.e. at $r = r_c$, are calculated on the basis of adsorption equilibrium with the bulk gas phase at partial pressures p_i at that position z and time t. The adsorption equilibrium can be calculated on the basis of the Ideal Adsorbed Solution Theory (IAST) of Myers and Prausnitz.[41] In applying the IAST, it is necessary to have reliable fits of the pure component isotherm data over a wide range of pressures; for this purpose, the dual-site Langmuir-Freundlich isotherm (1) are suitable for all guest molecules considered in this study. Intra-crystallite diffusion limitations will result in radial gradients of molar loadings within each crystallite particle, and we need to quantify these gradients.

For convenience, a set of equations describing the fixed bed adsorber are summarized in *Figure S24*. *Figure S25* provides a summary of key assumptions made in the adsorber simulations. *Figure S26* provides a summary of key numerical aspects of adsorber simulations. *Figure S27* presents a schematic diagram showing adsorption equilibrium thermodynamics using IAST.

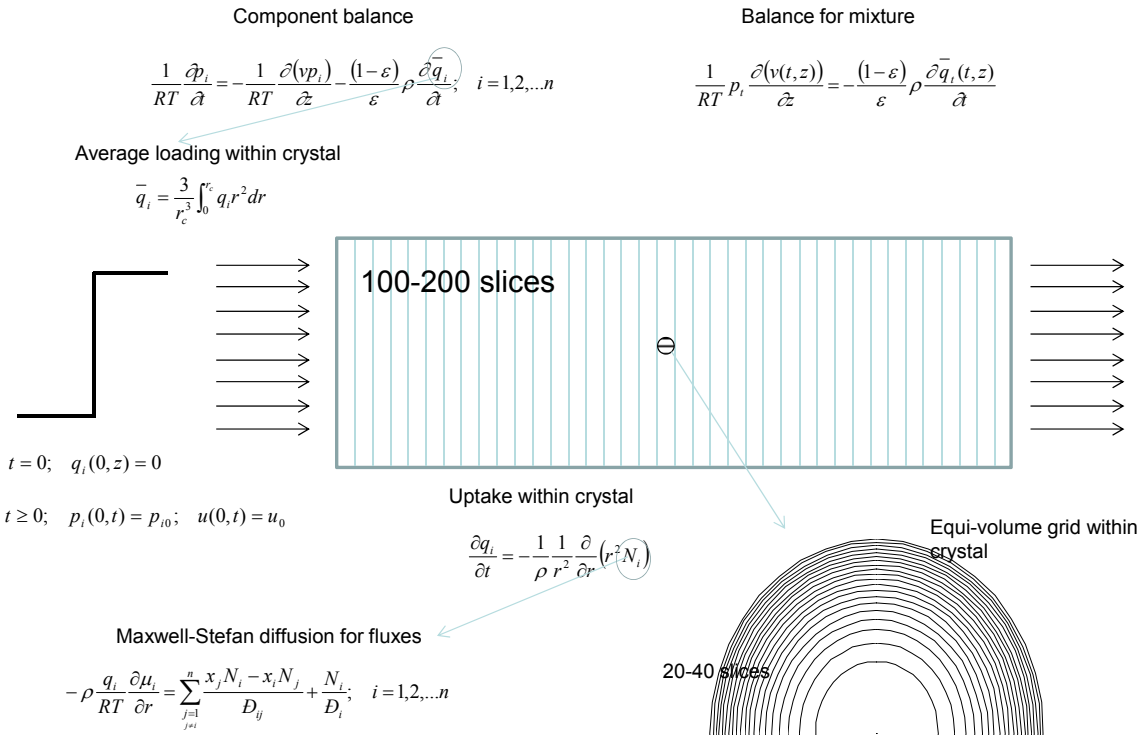

Figure S24. A summary of model equations describing a packed bed adsorber, along with discretization scheme.

- Negligible pressure drop, i.e. constant pressure
- Isothermal conditions, no heat effects
- Plug flow of gas mixture, i.e. no radial distribution of velocities and no axial dispersion
- At (t,z), the outer surface of the MOF crystallite is in thermodynamic equilibrium with the surrounding gas mixture at the corresponding position
- Adsorption equilibrium determined by rigorous IAST calculations using dual-Langmuir-Freundlich fits of measured experimental isotherms
- Diffusion within the crystallite is described by rigorous Maxwell-Stefan diffusion model for mixtures, accounting for correlation effects using MD simulations for the degree of correlations

Figure S25. A summary of key assumptions made in the adsorber simulations.

- 100-200 slices in adsorber
- 20-50 equi-volume elements within crystal for uptake simulations
- Combination of discretizated PDEs and algebraic IAST results in a set of differential algrebraic equations (DAEs)
- DAEs solved using Runge-Kutta, along with efficient sparse matrix solver incorporating the Bulirch-Stoer extrapolation
- The evaluation of the sparse Jacobian is by analytical expressions, making the computation times typically smaller than 200 s

Figure S26. A summary of key numerical aspects of adsorber simulations.

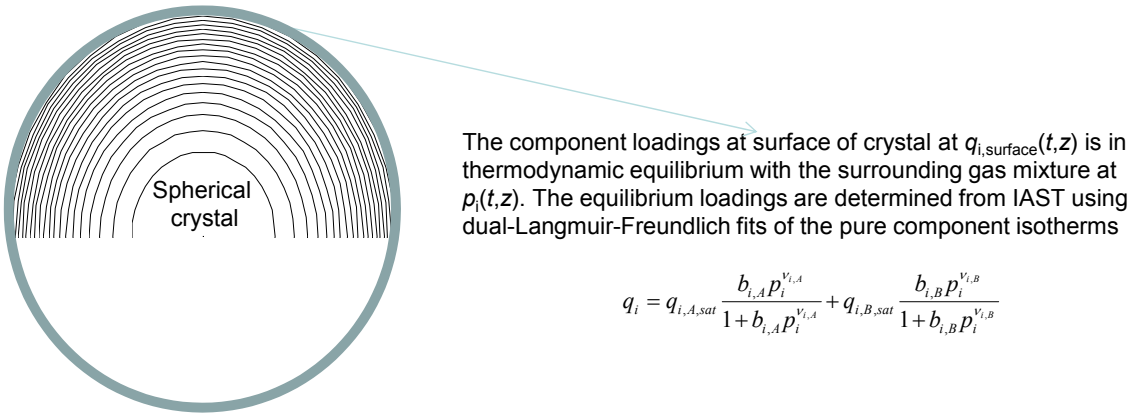

Figure S27. A schematic diagram showing adsorption equilibrium calculations using IAST.

Intra-crystalline diffusion and the Maxwell-Stefan equations

The radial distribution of molar loadings, q_i, within each crystallite is obtained from a solution of a set of differential equations describing the uptake within a crystallite:

$$\frac{\partial q_i}{\partial t} = -\frac{1}{\rho}\frac{1}{r^2}\frac{\partial}{\partial r}\left(r^2 N_i\right) \tag{9}$$

The fluxes N_i, in turn, are related to the radial gradients in the chemical potentials, $\partial\mu_i/\partial r$, by the Maxwell-Stefan (M-S) formulation of intra-crystalline diffusion.[33, 42-44]

$$-\rho\frac{q_i}{RT}\frac{\partial\mu_i}{\partial r} = \sum_{\substack{j=1\\ j\neq i}}^{n}\frac{x_j N_i - x_i N_j}{Đ_{ij}} + \frac{N_i}{Đ_i}; \quad i = 1,2,...n \tag{10}$$

where the mole fractions of the adsorbed phase, x_i, are defined as

$$x_i = \frac{q_i}{q_1 + q_2 + ...q_n} = \frac{q_i}{q_t} \quad i = 1,2,...n \tag{11}$$

The $Đ_i$ characterizes species i – wall interactions in the broadest sense. In many cases the $Đ_i$ corresponds to the value of the pure component i; consequently, this can be estimated from unary permeation data. In some cases where molecular clustering occurs, the $Đ_i$ in the mixture can be lower than that of pure components.[45, 46] The $Đ_{ij}$ is exchange coefficient representing interaction between components i with component j. At the molecular level, the $Đ_{ij}$ reflects how the facility for transport of species i *correlates* with that of species j. Conformity with the Onsager reciprocal relations prescribes

$$Đ_{ij} = Đ_{ji} \tag{12}$$

In the M-S formulation (10) the exchange coefficients $Đ_{ij}$ account for slowing-down effects, that are of vital importance in mixture diffusion.[47]

The chemical potential gradients in equation (10) can be related to the more conventional gradients of molar loadings by defining thermodynamic correction factors Γ_{ij}

$$\frac{q_i}{RT}\frac{\partial\mu_i}{\partial r} = \sum_{j=1}^{n}\Gamma_{ij}\frac{\partial q_j}{\partial r}; \quad \Gamma_{ij} = \frac{q_i}{p_i}\frac{\partial p_i}{\partial q_j}; \quad i,j = 1,2,...n \tag{13}$$

The elements of thermodynamic correction factors, Γ_{ij}, can be determined by differentiation of the dual-site Langmuir-Freundlich isotherm (1).

Figure S28 summarizes the Maxwell-Stefan diffusion equations used to describe intra-crystalline diffusion.

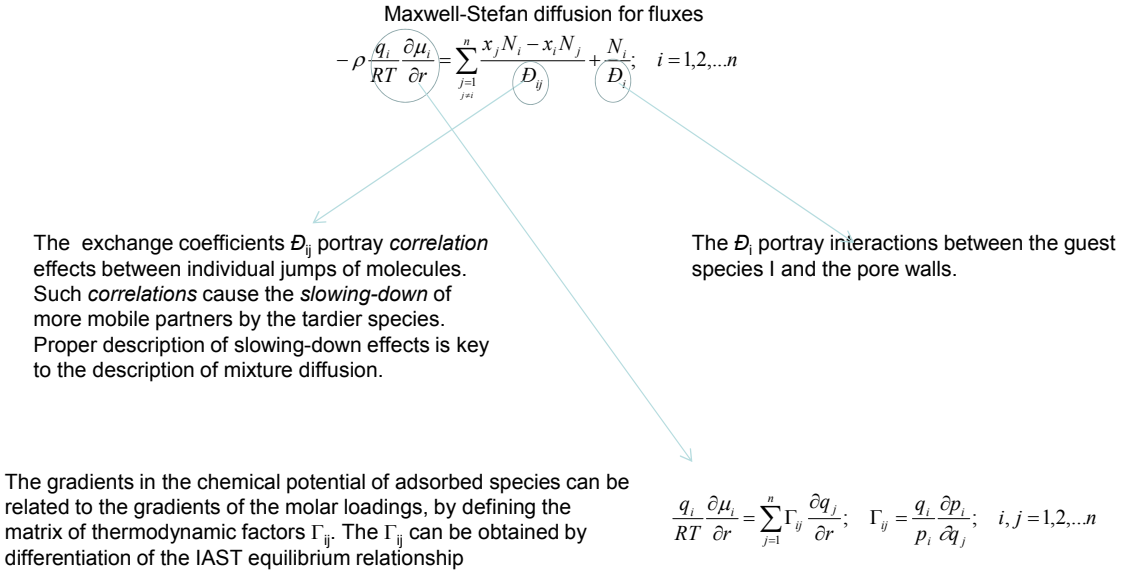

Figure S28. A schematic summary of the Maxwell-Stefan diffusion equations.

Fixed bed adsorber simulations with step inputs

In industrial practice, the most common operation is with to use a step-wise input of hydrocarbon mixtures to be separation into an adsorber bed that is initially free of adsorbates, i.e. we have the initial condition

$$t = 0; \quad q_i(0,z) = 0 \tag{11}$$

At time, t = 0, the inlet to the adsorber, z = 0, is subjected to a step input of the n-component gas mixture and this step input is maintained till the end of the adsorption cycle when steady-state conditions are reached.

$$t \geq 0; \quad p_i(0,t) = p_{i0}; \quad u(0,t) = u_0 \tag{12}$$

where u_0 is the superficial gas velocity at the inlet to the adsorber.

Figure S29a provides a schematic representation of the step input simulations. In all breakthrough calculations presented below, the following parameter values were used for all simulation data presented in this work: L = 0.12 m; ε = 0.75; u = 0.00225 m s^{-1}. It is to be noted that the actual values of these parameters have no bearing on the results for the production capacity presented later in this document. The simulation results for transient breakthrough are presented in our investigation in terms of a *dimensionless* time, τ, defined by dividing the actual time, t, by the characteristic time, $\frac{L\varepsilon}{u_0}$.

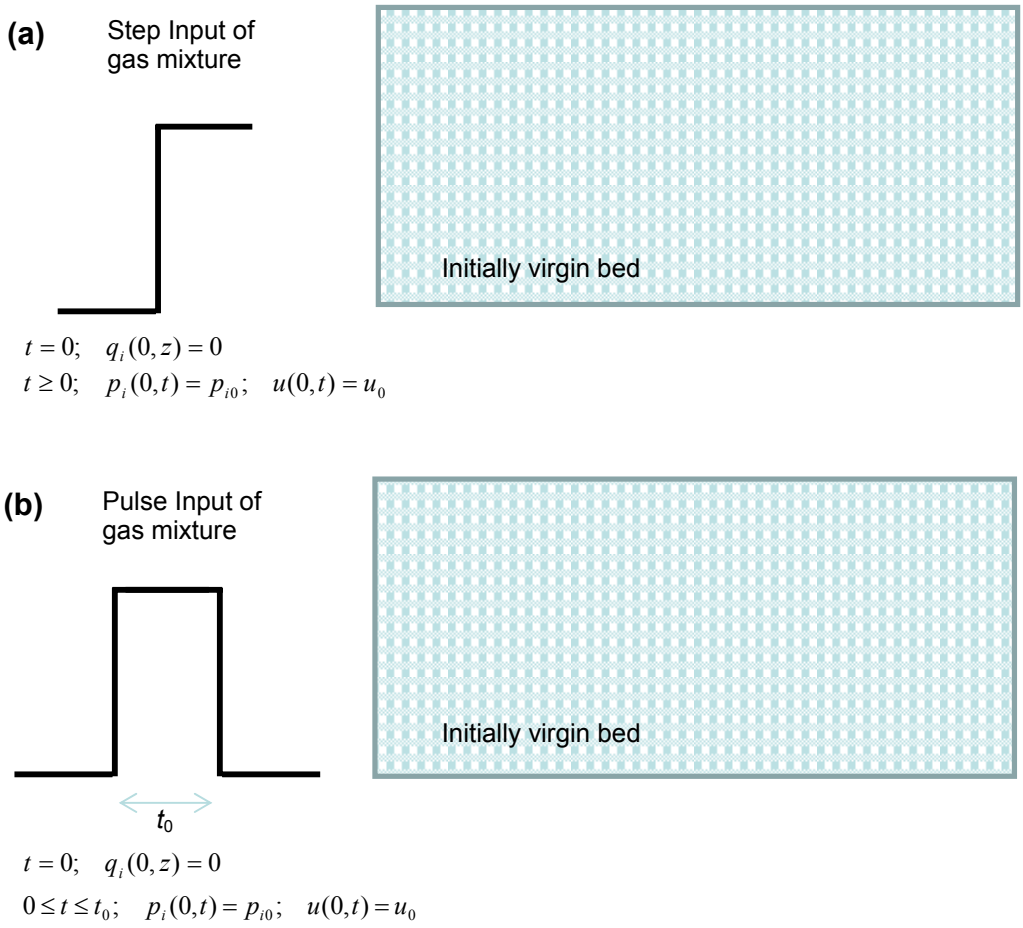

Figure S29. Two different types of breakthrough simulations. (a) step input of hydrocarbon mixtures to an initially virgin bed of adsorbent materials. (b) pulse chromatographic input of hydrocarbon mixtures.

Fixed bed adsorber simulations with pulse inputs

Besides the breakthrough simulations with a step-input (12), we also carried out simulations for a packed bed adsorber with injection of a short duration pulse of the mixture to be separated. This type of simulation is particularly useful to demonstrate the fractionating capability of adsorbents. In the US patent of Matzger et al.[20], pulse chromatographic experimental data are presented for **CoMOF-74** and **NiMOF-74** to demonstrate their potential for fractionation of ethylene/ethane and propylene/propane mixtures. For simulation of pulse chromatographic separations, we use the corresponding set of inlet conditions

$$0 \leq t \leq t_0;\quad p_i(0,t) = p_{i0};\quad u(0,t) = u_0 \qquad (13)$$

where the time for duration of the pulse is t_0. These pulse chromatographic simulations have the advantage of making the "fractionating" capability of a specific MOF to become evident visually.

Figure S29b provides a schematic representation of the pulse input simulations. For the pulse chromatographic simulations, the following parameter values were used, as before, L = 0.12 m; ε = 0.75; u = 0.00225 m s^{-1}, together with a pulse duration t_0 = 10 s.

Discretization and numerical procedures

Equations (3) and (9) are first subjected to finite volume discretization. Typically, the adsorber length L is divided into 100 or more slices. Each crystallite, assumed to be spherical, is divided into 10-20 equi-volume slices. The number of slices in each case is determined by checking that the obtained breakthrough results do not change on increasing it. In the cases where strong diffusional limitations are present, the intra-particle gradients of concentrations are steep and about 20-40 equi-volume slices within each crystallite need to be taken into consideration. Combination of the discretized PDEs along with the algebraic IAST equilibrium model, results in a set of differential-algebraic equations (DAEs), which are solved using BESIRK.[48] BESIRK is a sparse matrix solver, based on the semi-implicit Runge-Kutta method originally developed by Michelsen,[49] and extended with the Bulirsch-Stoer extrapolation method.[50] Use of BESIRK improves the numerical solution efficiency in solving the set of DAEs. The evaluation of the sparse Jacobian required in the numerical algorithm is largely based on analytic expressions.[33] Further details of the adsorber model, along with the numerical procedures used in this work, are provided by Krishna and co-workers.[33, 34, 51] Typical computation times for a binary gas mixture breakthrough are less than 500 s, allowing such transient adsorber calculations to be routinely used for screening purposes. For strong diffusional limitations, the computation times will increase due to increased number of intra-crystalline computational grids.

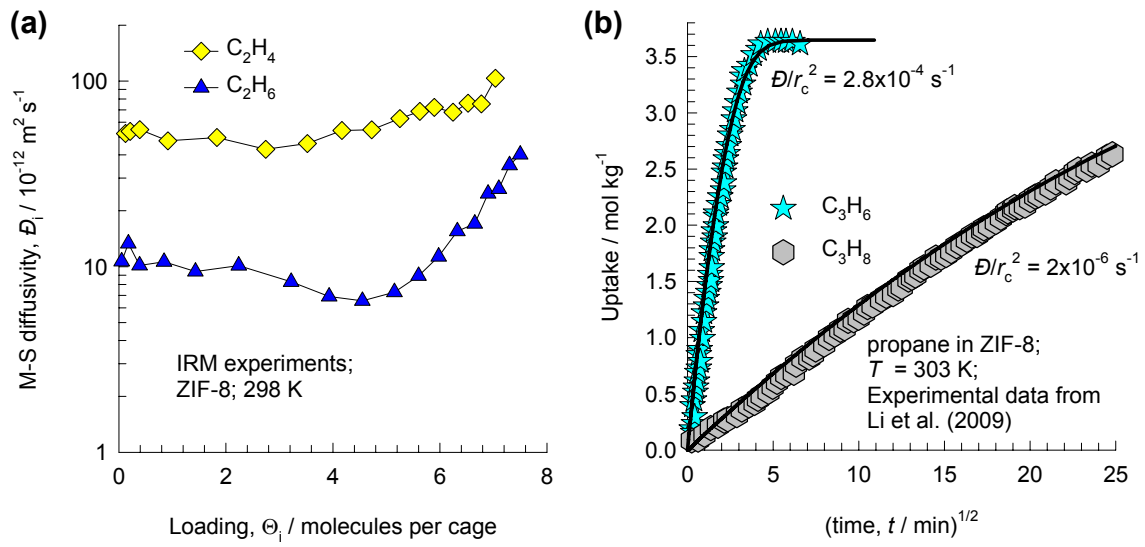

Figure S30. (a) Maxwell-Stefan diffusivities of C_2H_4, and C_2H_6 in **ZIF-8** at 298 K, measured by Infra-Red Microscopy.[26, 52-54] (b) Uptake of C_3H_6, and C_3H_8 within **ZIF-8** crystallites, measured at 303 K by Li et al.[27] The continuous solid lines are obtained from numerical solution of (4) and (9) using the parameter values as indicated for propylene and propane. Note: for **ZIF-8**, a loading of 1 molecule per cage corresponds to 0.73 mol/kg.

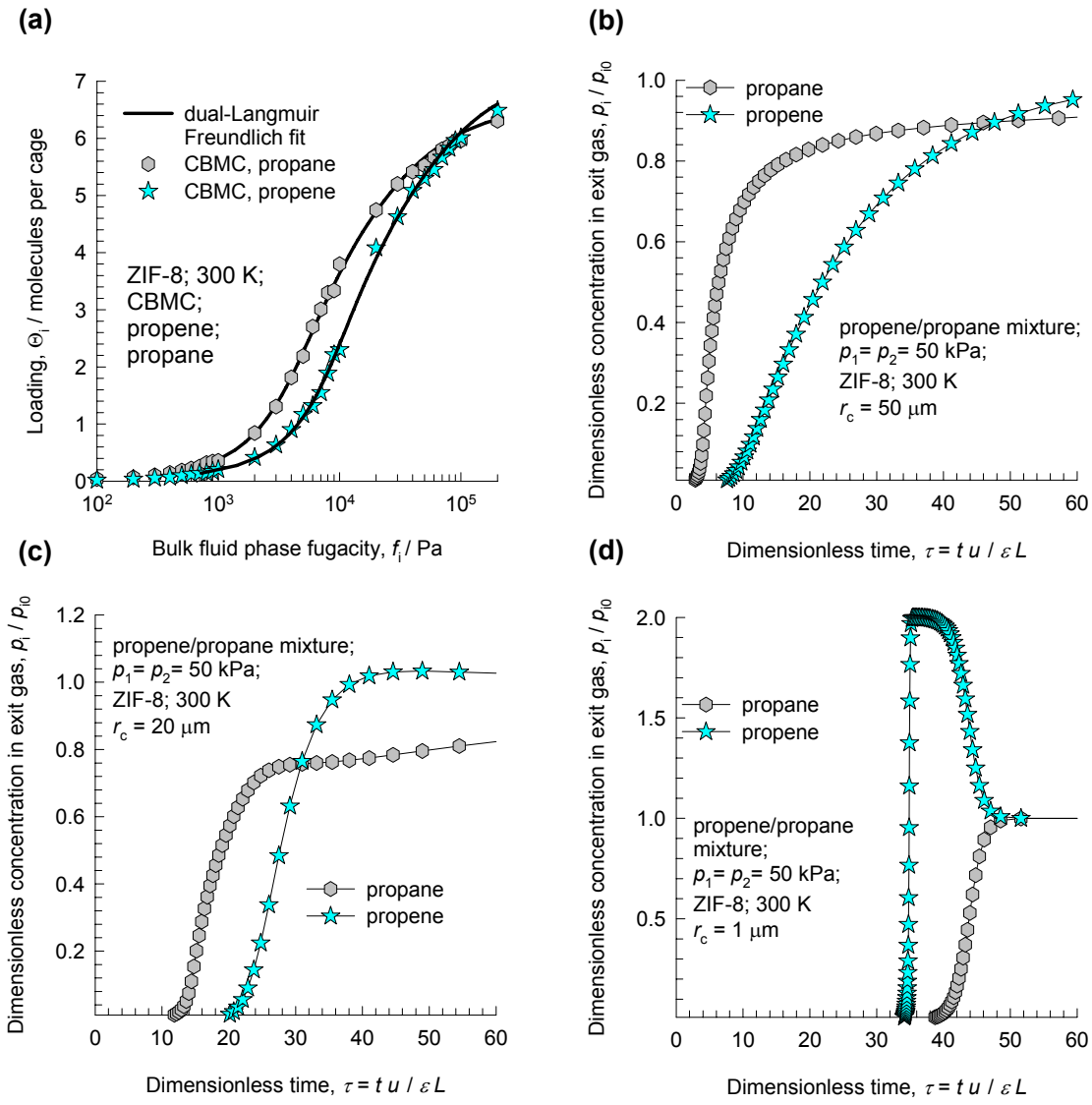

Figure S31. (a) Configurational-Bias Monte Carlo (CBMC) simulations[53] of the isotherms of C_3H_6, and C_3H_8 in **ZIF-8** at 300 K. (b-d) Transient breakthrough simulations for *equimolar* mixtures of C_3H_6, and C_3H_8 in packed bed adsorber operating at a total pressure of 100 kPa and 300 K, packed with **ZIF-8** crystallites with radii r_c of (b) 50 μm, (c) 20 μm, and (d) 1 μm. In the breakthrough simulations the values of the M-S diffusivities for C_3H_6, and C_3H_8 are taken to be $Đ_i = 5\times10^{-13}$ m^2 s^{-1}, and 1×10^{-14} m^2 s^{-1}, respectively. The simulations are carried out assuming constant diffusivity values, and neglecting thermodynamic correction factors on the diffusivity values.

Influence of diffusivities, and crystallite sizes

For use in packed bed adsorbers, the crystallites of MOFs, or ZIFs, typically with radii r_c in the range 50 μm – 200 μm are embedded into a macro-porous supporting (binder) material before being packed into an adsorber. The larger the crystallite size, the greater the influence of diffusion on the breakthrough characteristics.

The inclusion of diffusional effects is essential for alkene/alkane separations that are primarily based on diffusional, also termed "kinetic", selectivities. A good example of this is the separation of propylene and propane with **ZIF-8**. **ZIF-8** has the SOD zeolite topology and has cages separated by windows that are 3.26 Å in size. Small, subtle, differences in bond-lengths and bond angles cause the diffusivities of alkenes to be significantly lower than those of the corresponding alkanes. This is illustrated in the data of intra-crystalline diffusivities in **ZIF-8** obtained with Infra-Red Microscopy (IRM); see *Figure S30a*. The data show that the C_2H_4/C_2H_6 diffusion selectivity, in favor of C_2H_6, is in the range of 5 – 6, depending on the loading. Li et al.[27] report experimental data on uptake of C_3H_6, and C_3H_8 in **ZIF-**8 crystals; see *Figure S30b*. We note that the uptake of C_3H_6 proceeds much faster than for C_3H_8. The combination of equations (4) and (9) allows the determination of the transient uptake of components within MOF crystallites to be calculated. The measured uptake curves could be matched by choosing the values of $\frac{Đ_i}{r_c^2}$ = 2.8×10^{-4} s^{-1}, and 2×10^{-6} s^{-1}, for C_3H_6 and C_3H_8, respectively. The diffusion selectivity value of 140 in the uptake experiments of Li et al.[27]

The size of the crystallites that are embedded within the particles in the packed bed, has a significant bearing on the breakthrough characteristics of **ZIF-8**. In order to demonstrate the "kinetic" nature of the separation we carried out breakthrough simulations at 300 K, for a step-input of C_3H_6 /C_3H_8 50/50 gas mixtures at a total pressure of 100 kPa. The adsorption of C_3H_6 is poorer than that of C_3H_8 within **ZIF-8**; this is demonstrated by the Configurational-Bias Monte Carlo (CBMC) simulations[53] of the isotherms of C_3H_6, and C_3H_8 in **ZIF-8** at 300 K; the data is presented in *Figure S31a*. The dual-Langmuir Freundlich fits of the pure component isotherms were used, along with IAST calculations to determine the mixture adsorption equilibria. In the breakthrough simulations the values of the M-S diffusivities for C_3H_6, and C_3H_8 are taken to be $Đ_i$ = 5×10^{-13} m^2 s^{-1}, and 1×10^{-14} m^2 s^{-1}, respectively. The simulation results for an adsorber bed packed with **ZIF-8** crystallites of crystallite radii r_c of 50 μm, 20 μm, and 1 μm are shown in Figures 31b,c,d. For r_c = 50 μm, the breakthrough of C_3H_8 occurs earlier because of the significantly lower diffusivity of the alkane. At the other extreme, for r_c = 1 μm the breakthrough of C_3H_6 occurs earlier because for this particle size the value of $\frac{Đ_i}{r_c^2}$ is large enough to ensure that intra-crystalline gradients are absent and the entire crystallite particle can be considered to be in thermodynamic equilibrium with the surrounding bulk gas phase at that time t, and position z of the adsorber

$$\bar{q}_i(t,z) = q_i(t,z) \qquad (14)$$

The loadings $q_i(t,z)$ can be determined by application of the IAST for equilibrium with the bulk gas phase at the partial pressures $p_i(t,z)$.

For MOFs with more "open" structures such as **MgMOF-74**, **CoMOF-74**, **FeMOF-74**, **CuBTC** and also for **NaX** zeolite, the intra-crystalline diffusivities are about 1-3 orders of magnitude higher than for **ZIF-8**. For all such "open" structures, the influence of intra-crystalline diffusion is not of significant importance in determining the breakthroughs in fixed bed adsorbers. Equation (14) presents a good representation of the breakthrough characteristics of such "open" structures that emerge as promise candidates for separation of light hydrocarbons. We now validate this conclusion by comparison with available experimental data.

7. Validation of simulation methodology for transient breakthrough in fixed bed adsorbers

Before proceeding with using breakthrough simulations, invoking Equation (14) to investigate the separation characteristics of different MOFs, we seek validation of the suggested methodology with published experimental data.

Propylene/Propane breakthrough in CuBTC adsorber at 313 K

We consider the transient breakthrough characteristics of C_3H_6, and C_3H_8 mixtures in a packed bed of **CuBTC** crystallites as reported in the experiments of Yoon et al.[21] for a temperature of 313 K; see *Figure S32a*. The transient breakthrough characteristics are reasonably well represented by breakthrough simulations in which intra-crystalline diffusion effects are considered to be negligible and Equation (14) is invoked; witness the comparisons between experiments and simulations presented.

We now analyze in further detail the influence of intra-crystalline diffusion on the transient breakthrough characteristics with CuBTC. For this purpose, we need the values of the intra-crystalline diffusivities. Wehring et al.[55] report experimental data on self-diffusivities of C_3H_6, and C_3H_8 within crystals of **CuBTC** in Table 2 of their paper. At a temperature of 313 K, the diffusivities for C_3H_6, and C_3H_8 are calculated to be $Đ_i$ = 1.7×10^{-11} m^2 s^{-1}, and 2×10^{-10} m^2 s^{-1}, respectively. These values are about 2 orders of magnitude higher than the corresponding values for **ZIF-8**. It is also remarkable that the diffusivity value for C_3H_6 is lower than for C_3H_8. The reason for this can be traced to the higher binding energy of C_3H_6 compared to that for C_3H_8. The isosteric heats of adsorption, $-Q_{st}$, can be taken to a reflection of the binding energy. The values of the isosteric heats of adsorption, $-Q_{st}$, for C_3H_6 and C_3H_8 in **CuBTC** are 43 and 31 kJ mol^{-1}, respectively (see Table 2 of Wehring et al.[55]).

In *Figure S32b* two scenarios for breakthrough simulation results are compared. The first scenario is the same as the one presented in *Figure 32a*, corresponding to equilibrium behaviors, without the influence of intra-crystalline diffusion. The second scenario is one in which the intra-crystalline

diffusion is accounted for in which the values of the M-S diffusivities for C_3H_6, and C_3H_8 are taken to $Đ_i = 1.7\times10^{-11}$ m^2 s^{-1}, and 2×10^{-10} m^2 s^{-1}, respectively. The crystallite radius r_c is assumed to be 400 μm; this represents the largest crystallite size that is likely to be used in practice. The two sets of simulations yield virtually identical values for breakthrough times. Inclusion of intra-crystalline diffusion makes the breakthrough of propylene slightly more diffuse *after* breakthrough has occurred. The conclusion to be drawn here is that the assumption of thermodynamic equilibrium is a good one to make in practice, and invoking the assumption Equation (14) is sufficient to capture the separation performance of fixed bed adsorbers for hydrocarbons separations with MOFs that have "open" structures, i.e. with large pore volumes.

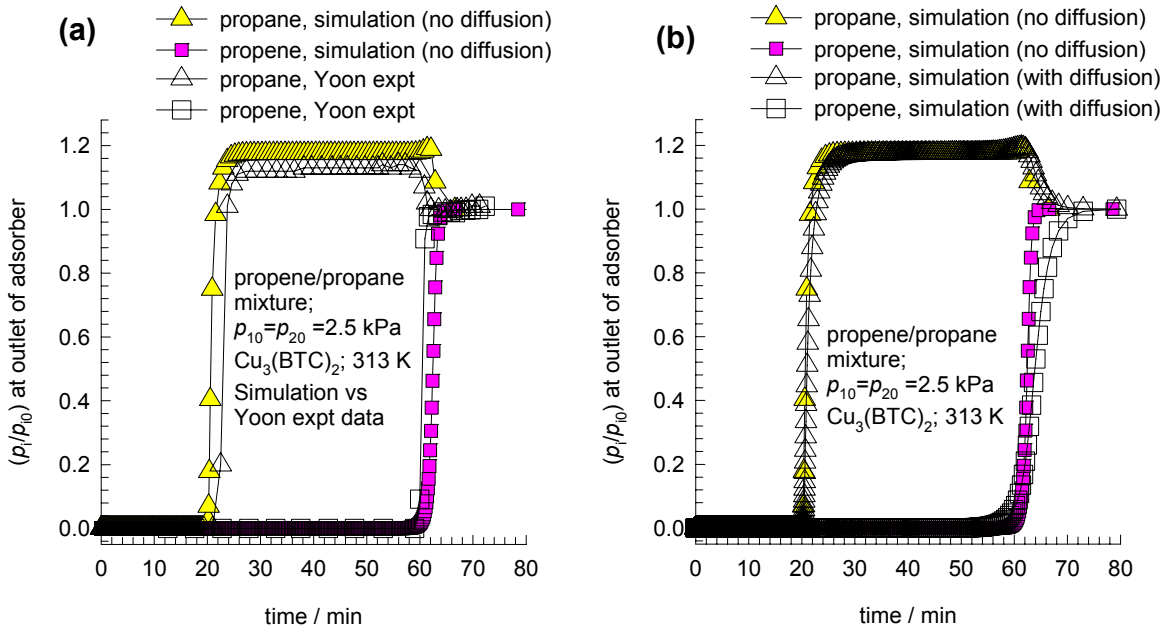

Figure S32. (a) Comparison of experimentally determined transient breakthrough for *equimolar* mixtures of C_3H_6, and C_3H_8 in packed bed adsorber operating at a total pressure of 100 kPa and 313 K, packed with **CuBTC** crystallites with *equilibrium based* simulations. The experimental data and chosen conditions are those presented by Yoon et al.[21] The inlet partial pressures of C_3H_6, and C_3H_8 are 2.5 kPa each; the remainder of the gas is made up of helium. In the breakthrough simulations the intra-crystalline diffusion is considered to be negligible and the assumption specified by Equation (14) is invoked. (b) Here two scenarios for breakthrough simulation results are compared. The first scenario is the same as the one presented in (a), corresponding to equilibrium behaviors, without the influence of intra-crystalline diffusion. The second scenario is one in which the intra-crystalline diffusion is accounted for in which the values of the M-S diffusivities for C_3H_6, and C_3H_8 are taken to $Đ_i = 1.7\times10^{-11}$ m^2 s^{-1}, and 2×10^{-10} m^2 s^{-1}, respectively. The crystallite radius r_c is assumed to be 400 μm. The simulations are carried out assuming constant diffusivity values, and neglecting thermodynamic correction factors on the diffusivity values.

Propylene/Propane breakthrough in FeMOF-74 adsorber at 318 K

In our investigations, **MgMOF-74**, **CoMOF-74**, and **FeMOF-74** emerge as the best materials for use in the wide variety of separations of light hydrocarbons. For any given guest molecule, the diffusivities

in each such structure will be nearly the same because the channel dimensions are virtually identical, corresponding to 1 nm. In the works of Bao et al.[17, 18], the diffusivities of uptake of a variety of guest molecules CO_2, CH_4, C_2H_4, C_2H_6, C_3H_6, and C_3H_8 in **MgMOF-74** were measured. As illustration, the transient uptake data for C_2H_4, C_2H_6, C_3H_6, and C_3H_8 in **MgMOF-74** at 298 K is shown in *Figure 33a*. In agreement with the data for **CuBTC** presented by Wehring et al.[55] , the diffusivity of the alkenes, are found to be lower than those of the corresponding alkane with the same C number. For example, the values of $\frac{Đ_i}{r_c^2}$ for C_3H_6, and C_3H_8 are $\frac{Đ_i}{r_c^2}$ = 3.14×10^{-3} s^{-1}, and 3.26×10^{-3} s^{-1}, for C_3H_6 and C_3H_8, respectively. We note that the value for C_3H_8 is about 3 orders of magnitude higher than the corresponding value for ZIF-8 obtained in the uptake experiments of Li et al.[27] The rationale for the lower diffusivity of the alkene in **MgMOF-74**, as compared to the alkane, can be traced to the fact that the alkene has a stronger binding energy, and consequently the higher "sticking" tendency leads to a lower diffusivity, as deduced from MD simulations in MgMOF-74.[51, 56] This explanation can be verified by plotting the values of $\frac{Đ_i}{r_c^2}$ as a function of the isosteric heats of adsorption, $-Q_{st}$, obtained in the limit of zero-loadings; see Figure *S33b*. The Q_{st} are those calculated in our work, and presented in *Figure 2* of the manuscript, in limit of zero-loading.

Breakthrough experiments were carried out by Bloch et al.[16] in a 4 mm tube packed with **FeMOF-74** crystallites; details of the experimental set-up and conditions are provided in the Supplementary Material accompanying their publication. The experimental breakthrough curves are in good agreement with simulations in which intra-crystalline diffusional effects are ignored, and equation (14) is invoked. The simulated transient gas composition profiles are in good agreement with the experimentally determined ones in *Figure S34*; this provides validation of the simulation methodology in which intra-crystalline diffusion effects are considered to be negligible.

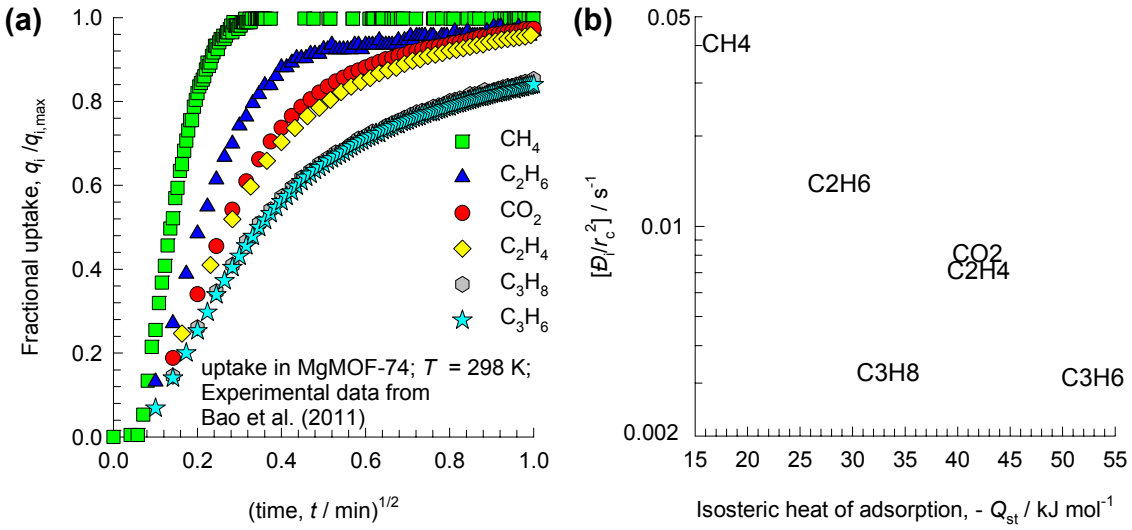

Figure S33. (a) Transient uptake of CH_4, CO_2, C_2H_4, C_2H_6, C_3H_6, and C_3H_8 in **MgMOF-74** at 298 K. The plotted data are from the experiments reported by Bao et al.[17, 18] (b) The values of $\frac{Đ_i}{r_c^2}$ of a variety of guest molecules CO_2, CH_4, C_2H_4, C_2H_6, C_3H_6, and C_3H_8 in **MgMOF-74** plotted as a function of the isosteric heats of adsorption, Q_{st}. The data for $\frac{Đ_i}{r_c^2}$ are those reported in the works of Bao et al.[17, 18] at a temperature of 298 K. The Q_{st} are those calculated in our work, and presented in *Figure 2* of the manuscript, in the limit of zero-loading. The Q_{st} data for CO_2 are obtained from the work of Mason et al.[57]

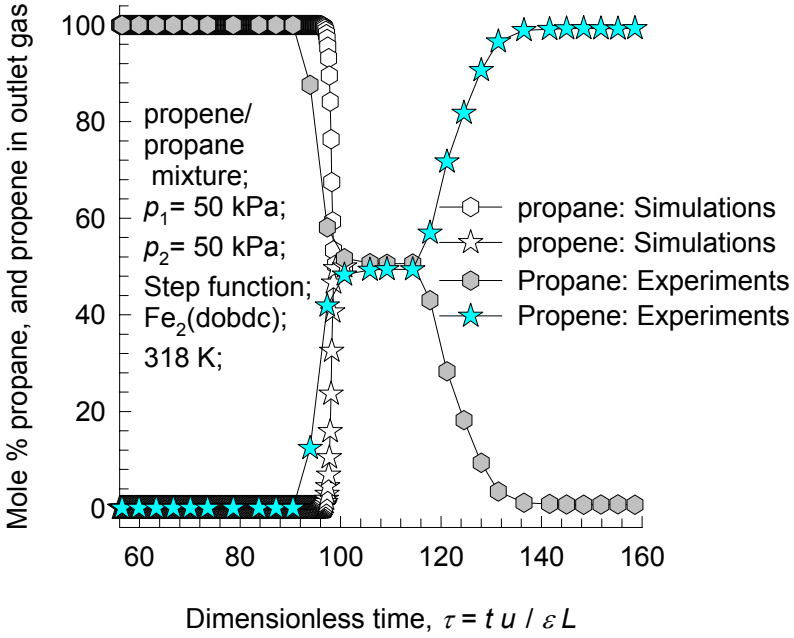

Figure S34. Comparison of experimentally determined transient breakthrough of an equimolar propylene/propane mixture in an adsorber bed packed with **FeMOF-74** at 318 K and a total pressure of 100 kPa with simulations in which the assumption specified by Equation (14) is invoked. Breakthrough experiments, reported by Bloch et al.[16] were carried out in a 4 mm tube packed with 375 mg of **FeMOF-74** crystallites. The crystallites were packed within 120 mm of the tube length, i.e. $L = 0.12$ m. The x-axis is the dimensionless time, obtained by dividing the actual time by the characteristic contact time, $\frac{L\varepsilon}{u_0}$.

Pulse chromatographic separations of alkene/alkane mixtures with CoMOF-74

The US patent awarded to Matzger et al.[20] presents pulse breakthrough experimental curves for separation of C_2H_4/C_2H_6 and C_3H_6/C_3H_8 mixtures in fixed beds packed with **CoMOF-74**; their data are reproduced in *Figure S35*.

These data clearly demonstrate the capability of **CoMOF-74** for fractionation of both mixtures. The corresponding pulse chromatographic simulations are shown in *Figure S36*. These simulations, using our isotherm data fits along with the assumption of negligible diffusional limitations is able to reproduce, albeit qualitatively, all the essential features of the pulse breakthroughs reported in the US patent.

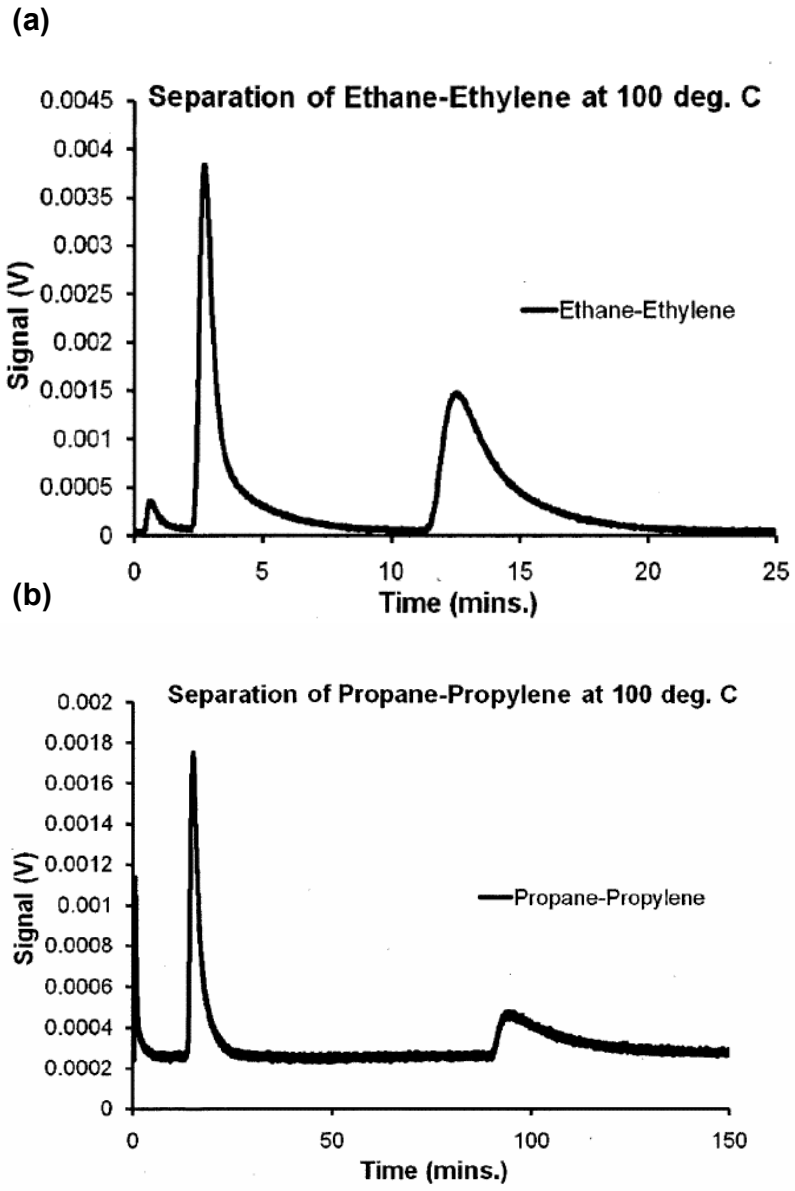

Figure S35. Pulse chromatographic experiments for (a) ethylene/ethane, and (b) propylene/propane separations as reported in the US patent awarded to Matzger et al.[20] The column is packed with **CoMOF-74**. No further details are provided in the patent.

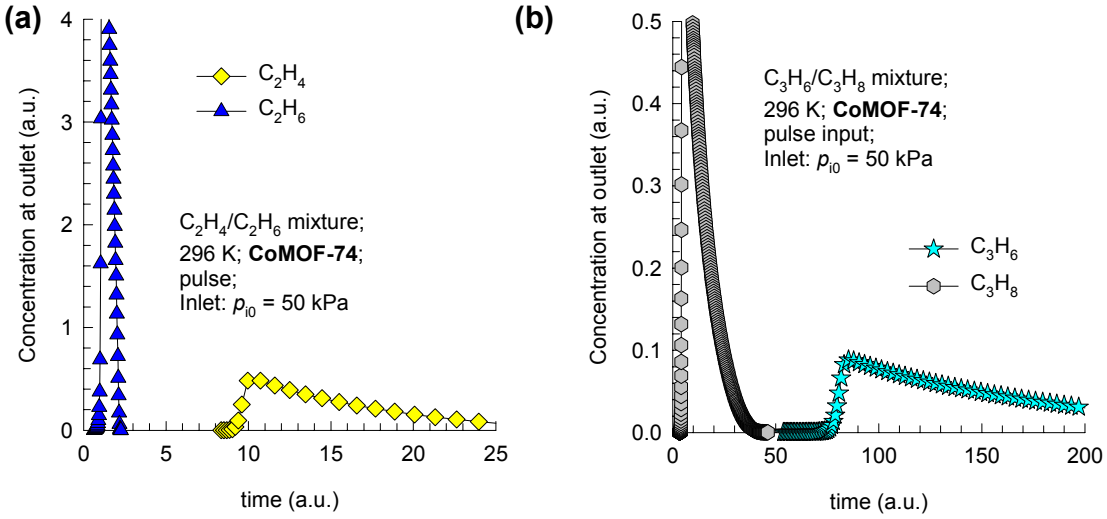

Figure S36. Pulse chromatographic simulations, neglecting intra-crystalline diffusion, for (a) ethylene/ethane and (b) propylene/propane separations with **CoMOF-74**. The inlet partial pressures in the pulse are taken to be 50 kPa each. Since the experimental details in the US patent awarded to Matzger et al.[20] are not provided, we have scaled the time scale to match the corresponding times shown in *Figure S35*.

8. Notation

b_A	dual-Langmuir-Freundlich constant for species *i* at adsorption site A, $Pa^{-\nu_i}$
b_B	dual-Langmuir-Freundlich constant for species *i* at adsorption site B, $Pa^{-\nu_i}$
$Đ_i$	Maxwell-Stefan diffusivity, $m^2\ s^{-1}$
$Đ_{ij}$	M-S exchange coefficient, $m^2\ s^{-1}$
L	length of packed bed adsorber, m
n	number of species in the mixture, dimensionless
N_i	molar flux of species *i*, mol $m^{-2}\ s^{-1}$
p_i	partial pressure of species *i* in mixture, Pa
p_{io}	partial pressure of species *i* at inlet to fixed bed, Pa
p_t	total system pressure, Pa
q_i	component molar loading of species *i*, mol kg^{-1}
$_i\bar{q}_i$	*spatially averaged* component molar loading of species *i*, mol kg^{-1}
q_t	total molar loading in mixture, mol kg^{-1}
$q_{sat,A}$	saturation loading of site A, mol kg^{-1}
$q_{sat,B}$	saturation loading of site B, mol kg^{-1}
Q_{st}	isosteric heat of adsorption, J mol^{-1}
r	radial direction coordinate, m
r_c	radius of crystallite, m
R	gas constant, 8.314 J $mol^{-1}\ K^{-1}$
S_{ads}	adsorption selectivity, dimensionless
t	time, s

t_0	duration of pulse, s
T	absolute temperature, K
u	superficial gas velocity in packed bed, m s^{-1}
u_0	superficial gas velocity at inlet to packed bed, m s^{-1}
v	interstitial gas velocity in packed bed, m s^{-1}
x_i	mole fraction of species *i* in adsorbed phase, dimensionless
z	distance along the adsorber, m

Greek letters

ε	voidage of packed bed, dimensionless
Γ_{ij}	thermodynamic factors, dimensionless
ϕ	fractional pore volume, dimensionless
μ_i	molar chemical potential, J mol^{-1}
ν	exponent in dual-Langmuir-Freundlich isotherm, dimensionless
ρ	framework density, kg m^{-3}
τ	time, dimensionless
τ_{break}	breakthrough time, dimensionless

Subscripts

0	referring to conditions at inlet to adsorber
i	referring to component *i*
A	referring to site A
B	referring to site B
t	referring to total mixture

9. References

1. Dietzel, P. D. C.; Morita, Y.; Blom, R.; Fjellvåg, H., An In Situ High-Temperature Single-Crystal Investigation of a Dehydrated Metal-Organic Framework Compound and Field-Induced Magnetization of One-Dimensional Metal-Oxygen Chains. *Angew. Chem. Int. Ed.* **2005,** 44, 6354-6358.
2. Dietzel, P. D. C.; Blom, R.; Fjellvåg, H., Base-Induced Formation of Two Magnesium Metal-Organic Framework Compounds with a Bifunctional Tetratopic Ligand. *Eur. J. Inorg. Chem.* **2008**, 3624-3632.
3. Caskey, S. R.; Wong-Foy, A. G.; Matzger, A. J., Dramatic Tuning of Carbon Dioxide Uptake via Metal Substitution in a Coordination Polymer with Cylindrical Pores. *J. Am. Chem. Soc.* **2008,** 130, 10870-10871.
4. Chui, S. S.-Y.; Lo, S. M.-F.; Charmant, J. P. H.; Orpen, A. G.; Williams, I. D., A Chemically Functionalizable Nanoporous Material $[Cu_3(TMA)_2(H_2O)_3]_n$. *Science* **1999,** 283, 1148-1150.
5. Chen, B.; Ockwig, N. W.; Millward, A. R.; Contreras, D. S.; Yaghi, O. M., High H_2 Adsorption in a Microporous Metal-Organic Framework with Open Metal Sites. *Angew. Chem. Int. Ed.* **2005,** 44, 4745-4749.
6. Hu, Y.; Xiang, S.; Zhang, W.; Zhang, Z.; Wang, L.; Bai, J.; Chen, B., A new MOF-505 analog exhibiting high acetylene storage. *Chem. Commun.* **2009**, 7551-7553.
7. Sun, D.; Ma, S.; Simmons, J. M.; Li, J.-R.; Yuan, D.; Zhou, H.-C., An unusual case of symmetry-preserving isomerism. *Chem. Commun.* **2010,** 46, 1329-1331.
8. Wong-Foy, A. G.; Lebel, O.; Matzger, A. J., Porous Crystal Derived from a Tricarboxylate Linker with Two Distinct Binding Motifs. *J. Am. Chem. Soc.* **2007,** 129, 15740-15741.
9. Lin, X.; Jia, J.; Zhao, X.; Thomas, K. M.; Blake, A. J.; Walker, G. S.; Champness, N. R.; Hubberstey, P.; Schröder, M., High H2 Adsorption by Coordination-Framework Materials. *Angew. Chem. Int. Ed.* **2006,** 45, 7358-7364.
10. Guo, Z.; Wu, H.; Srinivas, G.; Zhou, Y.; Xiang, S.; Chen, Z.; Yang, Y.; Zhou, W.; O'Keeffe, M.; Chen, B., A Metal-Organic Framework with Optimized Open Metal Sites and Pore Spaces for High Methane Storage at Room Temperature. *Angew. Chem. Int. Ed.* **2011,** 50, 3178-3181.
11. He, Y.; Zhang, Z.; Xiang, S.; Fronczek, F. R.; Krishna, R.; Chen, B., A Microporous Metal-Organic Framework for Highly Selective Separation of Acetylene, Ethylene and Ethane from Methane at Room Temperature. *Chem. Eur. J.* **2012,** 18, 613-619.
12. He, Y.; Zhang, Z.; Xiang, S.; Wu, H.; Fronczek, F. R.; Zhou, W.; Krishna, R.; O'Keeffe, M.; Chen, B., High Separation Capacity and Selectivity of C_2 Hydrocarbons over Methane within a Microporous Metal-Organic Framework at Room Temperature. *Chem. Eur. J.* **2012,** 18, 1901-1904.
13. He, Y.; Zhang, Z.; Xiang, S.; Fronczek, F. R.; Krishna, R.; Chen, B., A robust doubly interpenetrated metal-organic framework constructed from a novel aromatic tricarboxylate for highly selective separation of small hydrocarbons. *Chem. Commun.* **2012**, 48, 6493-6495.
14. Xiang, S.; Zhang, Z.; Zhao, C.-G.; Hong, K.; Zhao, X.; Ding, D.-L.; Xie, M.-H.; Wu, C.-D.; Gill, R.; Thomas, K. M.; Chen, B., Rationally Tuned Micropores within Enantiopure Metal-Organic Frameworks for Highly Selective Separation of C_2H_2/C_2H_4. *Nature Commun.* **2011,** 2, 204.
15. Das, M. C.; Guo, Q.; He, Y.; Kim, J.; Zhao, C.-G.; Hong, K.; Xiang, S.; Zhang, Z.; Thomas, K. M.; Krishna, R.; Chen, B., Interplay of Metalloligand and Organic Ligand to Tune Micropores within Isostructural Mixed-Metal Organic Frameworks (M'MOFs) for Their Highly Selective Separation of Chiral and Achiral Small Molecules. *J. Am. Chem. Soc.* **2012**, 134, 8703-8710.
16. Bloch, E. D.; Queen, W. L.; Krishna, R.; Zadrozny, J. M.; Brown, C. M.; Long, J. R., Hydrocarbon Separations in a Metal-Organic Framework with Open Iron(II) Coordination Sites. *Science* **2012,** 335, 1606-1610.
17. Bao, Z.; Alnemrat, S.; Vasiliev, I.; Ren, Q.; Yu, L.; Lu, X.; Deng, S., Adsorption of Ethane, Ethylene, Propane and Propylene on a Magnesium-Based Metal-Organic Framework. *Langmuir* **2011,** 27, 13554-13562.
18. Bao, Z.; Yu, L.; Ren, Q.; Lu, X.; Deng, S., Adsorption of CO_2 and CH_4 on a magnesium-based metal organic framework. *J. Colloid and Interface Sci.* **2011,** 353, 549-556.

19. Dietzel, P. D. C.; Besikiotis, V.; Blom, R., Application of metal–organic frameworks with coordinatively unsaturated metal sites in storage and separation of methane and carbon dioxide. *J. Mater. Chem.* **2009,** 19, 7362-7370.
20. Matzger, A. J.; Wong-Foy, A. G.; Caskey, G. Microporous coordination polymers as novel sorbents for gas separaration. *U.S. Pat.* **2010**, 2010/0258004 A1.
21. Yoon, J. W.; Jang, I. T.; Lee, K.-Y.; Hwang, Y. K.; Chang, J.-S., Adsorptive Separation of Propylene and Propane on a Porous Metal-Organic Framework, Copper Trimesate. *Bull. Korean Chem. Soc.* **2010,** 31, 220-223.
22. Yoon, J. W.; Seo, Y. K.; Hwang, Y. K.; Chang, J. S.; Leclerc, H.; Wuttke, S.; Bazin, P.; Vimont, A.; Daturi, M.; Bloch, E.; Llewellyn, P. L.; Serre, C.; Horcajada, P.; Grenèche, J. M.; Rodrigues, A. E.; Férey, G., Controlled Reducibility of a Metal–Organic Framework with Coordinatively Unsaturated Sites for Preferential Gas Sorption. *Angew. Chem. Int. Ed.* **2010,** 49, 5949-5952.
23. Hyun, S. H.; Danner, R. P., Equiilbrium Adsorption of Ethane, Ethylene, Isobutane, Carbon Dioxide, and Their Binary Mixtures on 13X Molecular Sieves. *J. Chem. Eng. Data* **1982,** 27, 196-200.
24. Lamia, N.; Granato, M. A.; Gomes, P. S. A.; Grande, C. A.; Wolff, L.; Leflaive, P.; Leinekugel-le-Cocq, D.; Rodrigues, A. E., Propane/Propylene Separation by Simulated Moving Bed II. Measurement and Prediction of Binary Adsorption Equilibria of Propane, Propylene, Isobutane, and 1-Butene on 13X Zeolite. *Sep. Sci. and Technol.* **2009,** 44, 1485-1509.
25. Anson, A.; Wang, Y.; Lin, C. C. H.; Kuznicki, T. M.; Kuznicki, S. M., Adsorption of ethane and ethylene on modified ETS-10. *Chem. Eng. Sci.* **2008,** 63, 4171-4175.
26. Bux, H.; Chmelik, C.; Krishna, R.; Caro, J., Ethene/Ethane Separation by the MOF Membrane ZIF-8: Molecular Correlation of Permeation, Adsorption, Diffusion. *J. Membr. Sci.* **2011,** 369, 284-289.
27. Li, K.; Olson, D. H.; Seidel, J.; Emge, T. J.; Gong, H.; Zeng, H.; Li, J., Zeolitic Imidazolate Frameworks for Kinetic Separation of Propane and Propene. *J. Am. Chem. Soc.* **2009,** 131, 10368-10369.
28. Pan, Y.; Li, T.; Lestari, G.; Lai, Z., Effective Separation of Propylene/Propane Binary Mixtures by ZIF-8 Membranes. *J. Membr. Sci.* **2012,** 390-391, 93-98.
29. Krishna, R.; Long, J. R., Screening metal-organic frameworks by analysis of transient breakthrough of gas mixtures in a fixed bed adsorber. *J. Phys. Chem. C* **2011,** 115, 12941-12950.
30. Ho, M. T.; Allinson, G. W.; Wiley, D. E., Reducing the Cost of CO_2 Capture from Flue Gases Using Pressure Swing Adsorption. *Ind. Eng. Chem. Res.* **2008,** 47, 4883-4890.
31. Kumar, R., Pressure Swing Adsorption Process: Performance Optimum and Adsorbent Selection. *Ind. Eng. Chem. Res.* **1994,** 33, 1600-1605.
32. Krishna, R.; van Baten, J. M., A comparison of the CO_2 capture characteristics of zeolites and metal-organic frameworks. *Sep. Purif. Technol.* **2012,** 87, 120-126.
33. Krishna, R.; Baur, R., Modelling issues in zeolite based separation processes. *Sep.Purif. Technol.* **2003,** 33, 213-254.
34. Krishna, R.; Baur, R. Diffusion, Adsorption and Reaction in Zeolites: Modelling and Numerical Issues. http://www.science.uva.nl/research/cr/zeolite/ (Accessed 8 March 2011),
35. Ruthven, D. M., *Principles of Adsorption and Adsorption Processes*. John Wiley: New York, 1984; p 433 pp.
36. Ruthven, D. M.; Farooq, S.; Knaebel, K. S., *Pressure swing adsorption*. VCH Publishers: New York, 1994.
37. Yang, R. T., *Gas separation by adsorption processes*. Butterworth: Boston, 1987.
38. Do, D. D., *Adsorption analysis: Equilibria and kinetics*. Imperial College Press: London, 1998.
39. van den Broeke, L. J. P.; Krishna, R., Experimental Verification of the Maxwell-Stefan Theory for Micropore Diffusion. *Chem. Eng. Sci.* **1995,** 50, 2507-2522.
40. Walton, K. S.; LeVan, M. D., Consistency of Energy and Material Balances for Bidisperse Particles in Fixed-Bed Adsorption and Related Applications. *Ind. Eng. Chem. Res.* **2003,** 42, 6938-6948.
41. Myers, A. L.; Prausnitz, J. M., Thermodynamics of mixed gas adsorption. *A.I.Ch.E.J.* **1965,** 11, 121-130.
42. Krishna, R., Describing the diffusion of guest molecules inside porous structures. *J. Phys. Chem. C* **2009,** 113, 19756-19781.

43. Krishna, R.; van Baten, J. M., Insights into diffusion of gases in zeolites gained from molecular dynamics simulations. *Micropor. Mesopor. Mater.* **2008,** 109, 91-108.
44. Krishna, R.; van Baten, J. M., Onsager coefficients for binary mixture diffusion in nanopores. *Chem. Eng. Sci.* **2008,** 63, 3120-3140.
45. Krishna, R.; van Baten, J. M., Highlighting Pitfalls in the Maxwell-Stefan Modeling of Water-Alcohol Mixture Permeation across Pervaporation Membranes. *J. Membr. Sci.* **2010,** 360, 476-482.
46. Krishna, R.; van Baten, J. M., Mutual slowing-down effects in mixture diffusion in zeolites. *J. Phys. Chem. C* **2010,** 114, 13154-13156.
47. Krishna, R.; van Baten, J. M., Maxwell-Stefan modeling of slowing-down effects in mixed gas permeation across porous membranes. *J. Membr. Sci.* **2011,** 383, 289-300.
48. Kooijman, H. A.; Taylor, R., A dynamic nonequilibrium model of tray distillation columns. *A.I.Ch.E.J.* **1995,** 41, 1852-1863.
49. Michelsen, M., An efficient general purpose method of integration of stiff ordinary differential equations. *A.I.Ch.E.J.* **1976,** 22, 594-597.
50. Bulirsch, R.; Stoer, J., Numerical treatment of ordinary differential equations by extrapolation methods. *Numer. Math.* **1966,** 8, 1-14.
51. Krishna, R.; van Baten, J. M., Investigating the potential of MgMOF-74 membranes for CO_2 capture. *J. Membr. Sci.* **2011,** 377, 249-260.
52. Chmelik, C.; Bux, H.; Caro, J.; Heinke, L.; Hibbe, F.; Titze, T.; Kärger, J., Mass transfer in a nanoscale material enhanced by an opposing flux. *Phys. Rev. Lett.* **2010,** 104, 085902.
53. Chmelik, C.; van Baten, J. M.; Krishna, R., Hindering effects in diffusion of CO_2/CH_4 mixtures in **ZIF-8** crystals. *J. Membr. Sci.* **2012,** 397-398, 87-91.
54. Chmelik, C.; Kärger, J., In situ study on molecular diffusion phenomena in nanoporous catalytic solids. *Chem. Soc. Rev.* **2010,** 39, 4864-4884.
55. Wehring, M.; Gascon, J.; Dubbeldam, D.; Kapteijn, F.; Snurr, R. Q.; Stallmach, F., Self-Diffusion Studies in CuBTC by PFG NMR and MD Simulations. *J. Phys. Chem. C* **2010,** 114, 10527-10534.
56. Krishna, R.; van Baten, J. M., Investigating the validity of the Knudsen prescription for diffusivities in a mesoporous covalent organic framework. *Ind. Eng. Chem. Res.* **2011,** 50, 7083-7087.
57. Mason, J. A.; Sumida, K.; Herm, Z. R.; Krishna, R.; Long, J. R., Evaluating Metal-Organic Frameworks for Post-Combustion Carbon Dioxide Capture via Temperature Swing Adsorption. *Energy Environ. Sci.* **2011,** 3, 3030-3040.
58. Bae, Y.-S.; Lee, C. Y.; Kim, K. C.; Farha, O. K.; Nickias, P.; Hupp, J. T.; Nguyen, S. T.; Snurr, R. Q., High Propene/Propane Selectivity in Isostructural Metal–Organic Frameworks with High Densities of Open Metal Sites. *Angew. Chem. Int. Ed.* **2012,** 51, 1857-1860.

Table S3. Dual-site Langmuir-Freundlich fit parameters for **CuBTC** (= **HKUST-1** = $Cu_3(btc)_2$).

	Site A				Site B			
	$q_{A,sat}$ mol kg^{-1}	b_{A0} Pa$^{-\nu_i}$	E_A kJ mol^{-1}	ν_A dimensionless	$q_{B,sat}$ mol kg^{-1}	b_{B0} Pa$^{-\nu_i}$	E_B kJ mol^{-1}	ν_B dimensionless
C_2H_2	5.4	1.29×10^{-11}	40	1	10.4	4.26×10^{-11}	29	1
C_2H_4	5.1	1.38×10^{-11}	40	1	6.6	4.59×10^{-10}	23.6	1
C_2H_6	11.4	3.81×10^{-11}	31	1				
CH_4	7.4	1.15×10^{-9}	17.7	1				

Table S4. Dual-site Langmuir-Freundlich fit parameters for **MOF-505**.

	Site A				Site B			
	$q_{A,sat}$ mol kg^{-1}	b_{A0} Pa$^{-\nu_i}$	E_A kJ mol^{-1}	ν_A dimensionless	$q_{B,sat}$ mol kg^{-1}	b_{B0} Pa$^{-\nu_i}$	E_B kJ mol^{-1}	ν_B dimensionless
C_2H_2	1.2	7.96×10^{-10}	34.2	1	9.8	7.62×10^{-11}	29	1
C_2H_4	0.64	3.35×10^{-12}	48	1	7	1.34×10^{-10}	29	1
C_2H_6	7.1	1.02×10^{-10}	31.5	1				
CH_4	10.8	3.34×10^{-10}	20	1				

Table S5. Dual-site Langmuir-Freundlich fit parameters for **PCN-16**.

	Site A				Site B			
	$q_{A,sat}$ mol kg^{-1}	b_{A0} Pa$^{-\nu_i}$	E_A kJ mol^{-1}	ν_A dimensionless	$q_{B,sat}$ mol kg^{-1}	b_{B0} Pa$^{-\nu_i}$	E_B kJ mol^{-1}	ν_B dimensionless
C_2H_2	3.4	3.09×10^{-12}	43.5	1	20.5	9×10^{-11}	25.5	1
C_2H_4	2.8	1.82×10^{-11}	39.4	1	12.6	1.03×10^{-9}	21.3	1
C_2H_6	19.8	1.98×10^{-10}	25	1				
CH_4	31	5.03×10^{-10}	15.5	1				

Table S6. Dual-site Langmuir-Freundlich fit parameters for **UMCM-150**.

	Site A				Site B			
	$q_{A,sat}$ mol kg^{-1}	b_{A0} Pa$^{-\nu_i}$	E_A kJ mol^{-1}	ν_A dimensionless	$q_{B,sat}$ mol kg^{-1}	b_{B0} Pa$^{-\nu_i}$	E_B kJ mol^{-1}	ν_B dimensionless
C_2H_2	2	2.97×10^{-12}	42.6	1	16.7	1.72×10^{-10}	24	1
C_2H_4	1.4	1.37×10^{-12}	44.6	1	12	2.86×10^{-10}	24	1
C_2H_6	24.6	1.28×10^{-10}	24.4	1				
CH_4	20.6	7.66×10^{-10}	15	1				

Table S7. Dual-site Langmuir-Freundlich fit parameters for **NOTT-101**.

	Site A				Site B			
	$q_{A,sat}$ mol kg^{-1}	b_{A0} Pa$^{-\nu_i}$	E_A kJ mol^{-1}	ν_A dimensionless	$q_{B,sat}$ mol kg^{-1}	b_{B0} Pa$^{-\nu_i}$	E_B kJ mol^{-1}	ν_B dimensionless
C_2H_2	2	2.58×10^{-11}	38.3	1	21	1.58×10^{-10}	25	1
C_2H_4	2.3	5.43×10^{-12}	41	1	14	2.95×10^{-10}	24	1
C_2H_6	32	2.37×10^{-9}	17.5	1				
CH_4	14	1.04×10^{-9}	16	1				

Table S8. Dual-site Langmuir-Freundlich fit parameters for **NOTT-102**.

	Site A				Site B			
	$q_{A,sat}$ mol kg^{-1}	b_{A0} Pa$^{-\nu_i}$	E_A kJ mol^{-1}	ν_A dimensionless	$q_{B,sat}$ mol kg^{-1}	b_{B0} Pa$^{-\nu_i}$	E_B kJ mol^{-1}	ν_B dimensionless
C_2H_2	2.5	2.21×10^{-8}	21	1	66	1.24×10^{-9}	15.5	1
C_2H_4	2.7	4.48×10^{-12}	41	1	23	2.28×10^{-10}	22	1
C_2H_6	52	1.44×10^{-10}	22.3	1				
CH_4	9.7	1.29×10^{-9}	16.2	1				

Table S9. Dual-site Langmuir-Freundlich fit parameters for **UTSA-20**.

	Site A				Site B			
	$q_{A,sat}$ mol kg^{-1}	b_{A0} Pa$^{-\nu_i}$	E_A kJ mol^{-1}	ν_A dimensionless	$q_{B,sat}$ mol kg^{-1}	b_{B0} Pa$^{-\nu_i}$	E_B kJ mol^{-1}	ν_B dimensionless
C_2H_2	2.1	2.26×10^{-11}	39.4	1	10	1.04×10^{-11}	33.6	1
C_2H_4	0.28	5.39×10^{-11}	43.8	1	6.67	3.9×10^{-11}	33	1
C_2H_6	8.1	4.46×10^{-11}	31	1				
CH_4	6.1	2.08×10^{-10}	21.7	1				

Table S10. Dual-site Langmuir-Freundlich fit parameters for **UTSA-33a**.

	Site A				Site B			
	$q_{A,sat}$ mol kg^{-1}	b_{A0} Pa$^{-\nu_i}$	E_A kJ mol^{-1}	ν_A dimensionless	$q_{B,sat}$ mol kg^{-1}	b_{B0} Pa$^{-\nu_i}$	E_B kJ mol^{-1}	ν_B dimensionless
C_2H_2	4	1.8×10^{-11}	26	1	5	2.18×10^{-11}	34	1
C_2H_4	3.7	7.2×10^{-11}	31	1	4.7	1.14×10^{-13}	37	1
C_2H_6	3.1	6.05×10^{-11}	33	1	1.6	1.19×10^{-12}	35	1
CH_4	3.3	1.01×10^{-10}	20.5	1	3.3	3.64×10^{-10}	20.5	1

Table S11. Dual-site Langmuir-Freundlich fit parameters for **UTSA-34a**.

	Site A				Site B			
	$q_{A,sat}$ mol kg^{-1}	b_{A0} Pa$^{-\nu_i}$	E_A kJ mol^{-1}	ν_A dimensionless	$q_{B,sat}$ mol kg^{-1}	b_{B0} Pa$^{-\nu_i}$	E_B kJ mol^{-1}	ν_B dimensionless
C_2H_2	1.1	9.68×10^{-11}	33	1	4.4	2.03×10^{-11}	33	1
C_2H_4	3.0	4.38×10^{-11}	33	1	1.6	4.44×10^{-12}	33	1
C_2H_6	2.2	1.18×10^{-10}	33	1	1.4	2.2×10^{-11}	35	1
CH_4	4.1	4.35×10^{-10}	20.6	1				

Table S12. Dual-site Langmuir-Freundlich fit parameters for **UTSA-34b**.

	Site A				Site B			
	$q_{A,sat}$ mol kg^{-1}	b_{A0} Pa$^{-\nu_i}$	E_A kJ mol^{-1}	ν_A dimensionless	$q_{B,sat}$ mol kg^{-1}	b_{B0} Pa$^{-\nu_i}$	E_B kJ mol^{-1}	ν_B dimensionless
C_2H_2	8	2.48×10^{-11}	32	1	1.2	1.75×10^{-14}	57	1
C_2H_4	5	1.13×10^{-10}	31	1	3.7	6.43×10^{-13}	36	1
C_2H_6	5.6	9.73×10^{-11}	31	1	0.74	1.33×10^{-12}	36	1
CH_4	6.8	3.96×10^{-10}	20	1				

Table S13. Dual-site Langmuir-Freundlich fit parameters for **UTSA-35a**.

	Site A				Site B			
	$q_{A,sat}$ mol kg^{-1}	b_{A0} Pa$^{-\nu_i}$	E_A kJ mol^{-1}	ν_A dimensionless	$q_{B,sat}$ mol kg^{-1}	b_{B0} Pa$^{-\nu_i}$	E_B kJ mol^{-1}	ν_B dimensionless
C_2H_2	5.05	9.7×10^{-11}	28	1	0.5	1.04×10^{-9}	31	1
C_2H_4	4	1.13×10^{-10}	28	1	0.5	6.43×10^{-13}	28	1
C_2H_6	3.65	8.45×10^{-11}	30	1	0.1	9.02×10^{-10}	30	1
CH_4	4	1.12×10^{-9}	17..2	1				
C_3H_6	1.8	3.78×10^{-9}	21.5	1	2.1	3.28×10^{-10}	34	1
C_3H_8	1.1	9.37×10^{-12}	36	1	2.25	1.22×10^{-11}	42	1

Table S14. Dual-site Langmuir-Freundlich fit parameters for **M'MOF-2a**.

	Site A				Site B			
	$q_{A,sat}$ mol kg^{-1}	b_{A0} Pa$^{-\nu_i}$	E_A kJ mol^{-1}	ν_A dimensionless	$q_{B,sat}$ mol kg^{-1}	b_{B0} Pa$^{-\nu_i}$	E_B kJ mol^{-1}	ν_B dimensionless
C_2H_2	1.8	7.18×10^{-9}	19	1	0.8	1.02×10^{-10}	36	1
C_2H_4	1.35	2.03×10^{-9}	21.7	1	0.5	1.55×10^{-10}	33.4	1

Table S15. Dual-site Langmuir-Freundlich fit parameters for **M'MOF-3a**.

	Site A				Site B			
	$q_{A,sat}$ mol kg^{-1}	b_{A0} Pa$^{-\nu_i}$	E_A kJ mol^{-1}	ν_A dimensionless	$q_{B,sat}$ mol kg^{-1}	b_{B0} Pa$^{-\nu_i}$	E_B kJ mol^{-1}	ν_B dimensionless
C_2H_2	2.66	2.47×10^{-6}	5	0.91	0.81	1.8×10^{-8}	25	0.93
C_2H_4	0.24	3.23×10^{-14}	32	1.9	1.93	2.11×10^{-11}	32	0.825

Table S16. Dual-site Langmuir-Freundlich fit parameters for **M'MOF-4a**.

	Site A				Site B			
	$q_{A,sat}$ mol kg^{-1}	b_{A0} Pa$^{-\nu_i}$	E_A kJ mol^{-1}	ν_A dimensionless	$q_{B,sat}$ mol kg^{-1}	b_{B0} Pa$^{-\nu_i}$	E_B kJ mol^{-1}	ν_B dimensionless
C_2H_2	2.84	5.78×10^{-11}	28	1	0.32	1.15×10^{-10}	36	1
C_2H_4	0.27	2.71×10^{-12}	39	1.2	9.7	5.85×10^{-13}	37	0.81

Table S17. Dual-site Langmuir-Freundlich fit parameters for **M'MOF-5a**.

	Site A				Site B			
	$q_{A,sat}$ mol kg^{-1}	b_{A0} Pa$^{-\nu_i}$	E_A kJ mol^{-1}	ν_A dimensionless	$q_{B,sat}$ mol kg^{-1}	b_{B0} Pa$^{-\nu_i}$	E_B kJ mol^{-1}	ν_B dimensionless
C_2H_2	10.4	8.74×10^{-13}	31	1	1.5	4.91×10^{-14}	50	1
C_2H_4	0.96	6.53×10^{-15}	46.6	1.2				

Table S18. Dual-site Langmuir-Freundlich fit parameters for **M'MOF-6a**.

	Site A				Site B			
	$q_{A,sat}$ mol kg^{-1}	b_{A0} Pa$^{-\nu_i}$	E_A kJ mol^{-1}	ν_A dimensionless	$q_{B,sat}$ mol kg^{-1}	b_{B0} Pa$^{-\nu_i}$	E_B kJ mol^{-1}	ν_B dimensionless
C_2H_2	0.45	1.33×10^{-9}	30	1	3.8	5.35×10^{-10}	22.5	1
C_2H_4	7	2.24×10^{-10}	19	1	0.36	1.11×10^{-10}	31.5	1

Table S19. Dual-site Langmuir-Freundlich fit parameters for **M'MOF-7a**.

	Site A				Site B			
	$q_{A,sat}$ mol kg^{-1}	b_{A0} Pa$^{-\nu_i}$	E_A kJ mol^{-1}	ν_A dimensionless	$q_{B,sat}$ mol kg^{-1}	b_{B0} Pa$^{-\nu_i}$	E_B kJ mol^{-1}	ν_B dimensionless
C_2H_2	2.4	1.02×10^{-15}	49.6	1	0.8	1.07×10^{-13}	47	1
C_2H_4	3	6.83×10^{-8}	5.9	1	0.01	1×10^{-9}	7.6	1

Table S20. Dual-site Langmuir-Freundlich fit parameters for **MgMOF-74** (= **CPO-27-Mg** = Mg_2(dobdc)).

Our experimental isotherm data for C_2H_4 and C_2H_6 are in excellent agreement with those presented in the paper by Bao et al.[17] (measured at 278 K, 298 K, and 318 K); the fitted parameters reported below are obtained by combining *both* data sets. Our experimental isotherm data for CH_4 are in excellent agreement with those reported by Bao et al.[18] (measured at 278 K, 298 K, and 318 K), and by Dietzel et al.[19] (measured at 283 K, 298K, 313 K, and 343 K); the parameter values are obtained by fitting all *three* data sets. The parameters for C_3H_6 and C_3H_8 are obtained by re-fitting the experimental isotherms of Bao et al.[17] (measured at 278 K, 298 K, and 318 K).

	Site A				Site B			
	$q_{A,sat}$ mol kg^{-1}	b_{A0} Pa$^{-\nu_i}$	E_A kJ mol^{-1}	ν_A dimensionless	$q_{B,sat}$ mol kg^{-1}	b_{B0} Pa$^{-\nu_i}$	E_B kJ mol^{-1}	ν_B dimensionless
C_2H_2	6.3	4.62×10^{-11}	41	1	8.4	8.43×10^{-11}	26	1
C_2H_4	3.1	2.15×10^{-12}	28	1.3	6.4	2.11×10^{-12}	45.2	1.07
C_2H_6	8.4	3.28×10^{-12}	34.5	1.2				
CH_4	11	7.48×10^{-10}	18.2	1	5	1.64×10^{-11}	18.2	1
C_3H_6	7.1	6.32×10^{-13}	55	1.04	1.7	2.17×10^{-14}	40	1.44
C_3H_8	1.9	2.22×10^{-11}	42	0.73	5.9	7.84×10^{-13}	42	1.41

Table S21. Dual-site Langmuir-Freundlich fit parameters for **CoMOF-74** (= **CPO-27-Co** = Co_2(dobdc)).

Our experimental isotherm data for C_2H_4 and C_2H_6 at 296 K are in good agreement with those presented in the papers by Bae et al.[58] (measured at 298 K), and reported in the US patent of Matzger et al.[20] (measured at 298 K); the fitted parameters reported below are obtained by all *three* data sets.

	Site A				Site B			
	$q_{A,sat}$ mol kg^{-1}	b_{A0} Pa$^{-\nu_i}$	E_A kJ mol^{-1}	ν_A dimensionless	$q_{B,sat}$ mol kg^{-1}	b_{B0} Pa$^{-\nu_i}$	E_B kJ mol^{-1}	ν_B dimensionless
C_2H_2	5.7	1.42×10^{-11}	45	1	9	2×10^{-10}	23.6	1
C_2H_4	5.2	5.23×10^{-10}	19.5	1	6.3	3.16×10^{-11}	41	1
C_2H_6	7.5	2.11×10^{-12}	37	1.2				
CH_4	7	3.74×10^{-11}	24.7	1	12.7	4.15×10^{-10}	17.8	1
C_3H_6	4.9	7.18×10^{-13}	54	1.16	2.3	3.55×10^{-13}	56	0.5
C_3H_8	1.3	3.27×10^{-14}	47	1	4.8	3.97×10^{-12}	47	1

Table S22. Dual-site Langmuir-Freundlich fit parameters for pure ethyne, ethylene, ethane, methane, propylene, and propane isotherms in **FeMOF-74** (= Fe_2(dobdc)) obtained by re-fitting the experimental isotherms of Bloch et al.[16] measured at 318 K, 333 K, and 353 K. These parameters are valid only within the temperature range of 318 K – 353 K; extrapolation to temperatures outside this range is not justified.

	Site A				Site B			
	$q_{A,sat}$ mol kg^{-1}	b_{A0} Pa$^{-\nu_i}$	E_A kJ mol^{-1}	ν_A dimensionless	$q_{B,sat}$ mol kg^{-1}	b_{B0} Pa$^{-\nu_i}$	E_B kJ mol^{-1}	ν_B dimensionless
C_2H_2	4.8	2.42×10^{-12}	51.4	1.1	3.2	2.07×10^{-10}	33.4	0.89
C_2H_4	1.74	6.51×10^{-12}	38	1.12	4.9	4.16×10^{-13}	53	1.12
C_2H_6	8.42	4.47×10^{-11}	31	1.1				
CH_4	6.7	8.06×10^{-10}	19.6	1				
C_3H_6	5.3	1.42×10^{-20}	97	1.76	1.7	1.29×10^{-10}	33	1.13
C_3H_8	2.1	5.95×10^{-12}	48	0.83	4.3	6.15×10^{-15}	53	1.63

Table S23. Dual-site Langmuir-Freundlich fit parameters for propylene and propane isotherms in **CuBTC** (= $Cu_3(btc)_2$) using the simultaneous fits of the experimental isotherm data in the paper of Yoon et al.[21], measured at temperatures of 303 K, 313 K, 323 K, 333 K, and 353 K.

	Site A				Site B			
	$q_{A,sat}$ mol kg^{-1}	b_{A0} Pa$^{-\nu_i}$	E_A kJ mol^{-1}	ν_A dimensionless	$q_{B,sat}$ mol kg^{-1}	b_{B0} Pa$^{-\nu_i}$	E_B kJ mol^{-1}	ν_B dimensionless
C_3H_6	5.8	1.85×10^{-10}	37.3	0.95	3.25	3.64×10^{-14}	59	1.25
C_3H_8	4.9	1.06×10^{-7}	25	0.62	4.0	1.45×10^{-22}	75	2.43

Table S24. Single-site Langmuir-Freundlich fit parameters for propylene and propane isotherms in **FeMIL-100** at 303 K. The parameter fits are based on fitting the data provided in Figure 2 of the paper by Yoon et al.[22]

	$q_{i,A,sat}$ mol/kg	$b_{i,A}$ Pa$^{-\nu_i}$	$\nu_{i,A}$ dimensionless
C_3H_6	2.1	6.21×10^{-3}	0.64
C_3H_8	7	1.53×10^{-5}	1

Table S25. Dual-site Langmuir fit parameters for pure ethylene and pure ethane isotherms in **NaX** zeolite using simultaneous fits the experimental data from Hyun and Danner [23] measured at 273 K, 298 K, and 323 K. The isotherm fits were used to determine the performance of **NaX** at a temperature of 296 K for comparison with different MOFs.

	Site A				Site B			
	$q_{A,sat}$ mol kg^{-1}	b_{A0} Pa$^{-\nu_i}$	E_A kJ mol^{-1}	ν_A dimensionless	$q_{B,sat}$ mol kg^{-1}	b_{B0} Pa$^{-\nu_i}$	E_B kJ mol^{-1}	ν_B dimensionless
C_2H_4	0.75	2.09×10^{-10}	40	1	2.15	9.28×10^{-11}	35	1
C_2H_6	2.95	3.07×10^{-10}	28.7	1				

Table S26. Dual-site Langmuir fit parameters for propylene and propane isotherms in **NaX** zeolite at 298 K, and 318 K. The parameter fits are based on re-fitting the data provided in Table 4 of the paper by Lamia et al [24].

At 298 K, the parameters are:

	Site A			Site B		
	$q_{i,A,sat}$ mol/kg	$b_{i,A}$ Pa$^{-\nu_i}$	$\nu_{i,A}$ dimensionless	$q_{i,B,sat}$ mol/kg	$b_{i,B}$ Pa$^{-\nu_i}$	$\nu_{i,B}$ dimensionless
C_3H_6	1.1	1.28×10^{-2}	1	1.44	1.03×10^{-3}	1
C_3H_8	1.1	1.13×10^{-3}	1	1.1	3.25×10^{-4}	1

At 318 K, the parameters are:

	Site A			Site B		
	$q_{i,A,sat}$ mol/kg	$b_{i,A}$ Pa$^{-\nu_i}$	$\nu_{i,A}$ dimensionless	$q_{i,B,sat}$ mol/kg	$b_{i,B}$ Pa$^{-\nu_i}$	$\nu_{i,B}$ dimensionless
C_3H_6	1.1	4.47×10^{-3}	1	1.44	3.4×10^{-4}	1
C_3H_8	1.1	1.28×10^{-4}	1	1.1	4.44×10^{-4}	1

Table S27. Dual-site Langmuir-Freundlich fit parameters for pure ethylene and ethane isotherms in **NaETS-10** zeolite, obtained by re-fitting the Toth isotherm parameters reported by Anson et al.[25] These parameters are valid only for 298 K; consequently, no E_A, and E_B parameter values are reported here.

	Site A				Site B			
	$q_{A,sat}$ mol kg^{-1}	b_{A0} Pa$^{-\nu_i}$	E_A kJ mol^{-1}	ν_A dimensionless	$q_{B,sat}$ mol kg^{-1}	b_{B0} Pa$^{-\nu_i}$	E_B kJ mol^{-1}	ν_B dimensionless
C_2H_4	0.68	5×10^{-2}		0.75	1.1	1.0×10^{-2}		0.6
C_2H_6	1	1.94×10^{-3}		0.72	0.44	9.96×10^{-3}		0.85

Table S28. IAST and breakthrough calculations for separation of an equimolar $CH_4/C_2H_2/C_2H_4/C_2H_6$ mixture at 296 K.

MOFs	IAST calculations		Breakthrough calculations	
	C_2H_6/CH_4 Adsorption selectivity	C_2H_2+C_2H_4+ C_2H_6 Uptake capacity mol L^{-1}	Dimensionless time interval $\Delta\tau$	99%+ pure CH_4 produced during $\Delta\tau$ mol L^{-1}
CoMOF-74	7.77	7.73	74.10	2.13
MgMOF-74	11.61	6.48	49.30	1.70
CuBTC (=HKUST-1)	17.42	6.09	44.50	1.41
MOF-505	16.30	4.63	41.34	1.28
PCN-16	10.73	4.49	34.88	1.05
UMCM-150	9.24	2.83	18.39	0.60
NOTT-101	11.68	4.18	31.27	0.95
NOTT-102	5.81	2.69	9.34	0.31
UTSA-20	15.44	4.46	31.90	1.11
UTSA-33a	14.88	2.69	25.96	0.70
UTSA-34a	19.08	2.37	19.40	0.62
UTSA-34b	16.11	3.49	27.50	0.95
UTSA-35a	13.54	2.20	18.37	0.55

Table S29. IAST and breakthrough calculations for separation of an equimolar C_2H_4/C_2H_6 mixture at $p_1 = p_2 = 50$ kPa, and $T = 296$ K. The data for **FeMOF-74** are at 318 K.

MOFs	IAST calculations		Breakthrough calculations			
			Adsorption cycle: 99%+ pure ethane production		Desorption cycle: 99.5%+ pure ethene production	
	C_2H_4/C_2H_6 Adsorption selectivity	C_2H_4 Uptake capacity mol L^{-1}	Dimensionless time interval $\Delta\tau_{ads}$	C_2H_6 produced during $\Delta\tau_{ads}$ mol L^{-1}	Dimensionless time interval $\Delta\tau_{des}$	C_2H_4 produced during $\Delta\tau_{des}$ mol L^{-1}
CoMOF-74	6.45	6.68	42.90	4.97	2379.00	4.47
MgMOF-74	5.63	5.41	35.50	3.97	1195.00	3.72
FeMOF-74	10.79	6.71	45.3	5.43	4506.00	4.98
CuBTC	3.63	4.76	29.63	2.97	525.31	2.60
PCN-16	2.77	0.22	16.04	1.46	255.50	1.32
NOTT-102	3.17	2.22	19.60	1.30	105.73	1.21
UTSA-20	1.96	2.95	10.85	1.06	299.42	0.86
NaX	8.01	3.37	25.03	2.71	1212.44	2.39
NaETS-10	14.78	2.99	22.30	2.42	2163.01	1.45

Table S30. IAST and breakthrough calculations for separation of an equimolar C_3H_6/C_3H_8 mixture at $p_1 = p_2 = 10$ kPa, and $T = 296$ K. The data for **FeMOF-74** is at 318 K. The data for **FeMIL-100** are at 303 K.

MOF	IAST calculations	Breakthrough calculations	
	C_3H_6/C_3H_8 Adsorption selectivity	Adsorption cycle: 99%+ pure propane production; C_3H_8 produced during $\Delta\tau_{ads}$ mol L^{-1}	Desorption cycle: 99.5%+ pure propene production; C_3H_6 produced during $\Delta\tau_{des}$ mol L^{-1}
CoMOF-74	8.63	4.38	3.48
MgMOF-74	10.67	4.80	3.27
FeMOF-74	13.68	5.39	3.64
CuBTC	4.95	4.26	3.53
NaX	9.27	2.50	1.40
FeMIL-100	4.33	0.57	0.48

Table S31. IAST and breakthrough calculations for separation of C_2H_2/C_2H_4 mixture containing 1 mol% C_2H_2 at 296 K. The product gas stream contains less than 40 ppm C_2H_2.

MOFs	IAST calculations		Breakthrough calculations	
	C_2H_2/C_2H_4 Adsorption selectivity	C_2H_2 Uptake capacity mmol L^{-1}	Dimensionless breakthrough time τ_{break}	C_2H_4 produced during 0 - τ_{break} mmol L^{-1}
CoMOF-74	1.62	129.84	74.40	89.66
MgMOF-74	2.23	148.44	85.65	103.33
MOF-505	1.45	68.39	40.05	48.00
UTSA-20	1.53	70.61	40.95	48.97
UTSA-33a	1.64	43.73	25.64	30.33
UTSA-34a	1.58	36.46	21.55	25.33
UTSA-34b	1.42	51.52	30.27	36.00
UTSA-35a	2.07	45.36	26.59	31.47
M'MOF-2a	3.12	38.15	22.52	26.53
M'MOF-3a	24.03	99.98	60.37	72.00
M'MOF-4a	14.31	72.23	41.86	50.00
M'MOF-5a	4.94	25.81	15.36	17.80
M'MOF-6a	7.42	48.52	28.95	34.33
M'MOF-7a	7.43	15.99	9.90	11.13